JETP Letters, Vol. 73, No. 3, 2001, pp. 115–117. Translated from Pis'ma v Zhurnal Éksperimental'noĭ i Teoreticheskoĭ Fiziki, Vol. 73, No. 3, 2001, pp. 131–133.

Yakutsk EAS Array Data on the Variations in Intensities of the Highest Energy Cosmic Rays

A. V. Glushkov* and M. I. Pravdin

Institute of Cosmophysical Research and Aeronomy, Yakut Research Center, Siberian Division, Russian Academy of Sciences, pr. Lenina 31, Yakutsk, 677891 Russia

** e-mail: a.v.glushkov@ikfia.ysn.ru*

Received October 20, 2000; in final form, December 7, 2000

The results of analysis of arrival frequency of cosmic rays with energies $E_0 \geq 4 \times 10^{17}$ eV are presented based on the data collected on the Yakutsk array during its 24 years of continuous operation (1977–2000). It is shown that the intensity of cosmic rays is variable. At $E_0 \leq (3\text{–}5) \times 10^{18}$ eV, the (2–3)-month data show many deviations by (3–4)σ from the mean level. At $E_0 \geq 10^{19}$ eV, the intensities steadily decrease, on the average, by 1.5 times during the time period considered. © *2001 MAIK "Nauka/Interperiodica".*

PACS numbers: 98.70.Sa; 95.85.Ry

1. INTRODUCTION

In spite of the fact that the highest energy cosmic rays ($E_0 \geq 10^{17}$ eV) have been studied worldwide on extensive air shower (EAS) arrays for more than 40 years, they remain an enigma. The primary particles with $E_0 \geq 10^{19}$ eV are the worst studied because their flux is exceedingly small. Their chemical composition remains a mystery, although it is hard to understand the character of nuclear interactions in this energy range without knowledge of this composition. According to the data [1–3], some new processes of EAS development occur at $E_0 \geq (3\text{–}5) \times 10^{18}$ eV.

The revelation of sources of ultrahigh energy cosmic ray may be helpful in solving this problem, although this approach also encounters many difficulties. Recent publications [4, 5] report the detection of clusters in the arrival directions of particles with $E_0 \geq 10^{19}$ eV. In [4], they were found to be associated with pulsars located on the entrance side of the local arm of the Galaxy. On the global scale, the particles with such energies do not contradict the isotropic distribution, although they give evidence for a certain correlation between the arrival directions and galactic (see, e.g., [6, 7]) and supergalactic [8, 9] planes.

It is shown in [9] that the excess cosmic ray flux from the side of the supergalactic plane varies with time. This work presents the experimental results that throw further light on the problem of variable intensity of ultrahigh energy cosmic rays.

2. CHARACTERISTICS UNDER INVESTIGATION AND DISCUSSIONS

In what follows, the EASs with energies $E_0 \geq 4 \times 10^{17}$ eV and zenith angles $\theta \leq 50°$, detected on the Yakutsk array during the period from 1977 to 2000, are considered. The EAS arrival frequencies are studied in several intervals ΔE_0 [(*a*) (0.4–1) $\times 10^{18}$, (*b*) (1–3) $\times 10^{18}$, (*c*) (3–10) $\times 10^{18}$, and (*d*) $\geq 10^{19}$ eV] having different local slopes of the primary energy spectrum (Fig. 1). The energy of primary particles was found from the relationships

$$E_0 = (4.8 \pm 1.6) \times 10^{17} (\rho(0°))^{1.0 \pm 0.02} \text{ [eV]}, \quad (1)$$

$$\rho(0°) = \rho(\theta) \exp((\sec\theta - 1) \times 1020/\lambda_\rho) \text{ [m}^{-2}\text{]}, \quad (2)$$

$$\lambda_\rho = (450 \pm 44) + (32 \pm 15) \log(\rho(0°)) \text{ [g/cm}^2\text{]}, \quad (3)$$

where $\rho(\theta)$ is the density of charged particles measured by surface scintillation detectors at a distance of R = 600 m from the shower axis.

Dark squares in Fig. 1 correspond to the energy spectrum measured on the AGASA array [11]. This array is similar to ours in the type of detectors, detection method, and data processing. One can see that both spectra are similar in shape at $E_0 \leq 6 \times 10^{19}$ eV to within experimental errors. We call attention to the fact that the spectra flatten in the energy range $E_0 \geq 10^{19}$ eV. The particles with $E_0 \sim 10^{20}$ eV need separate examination. They do not influence our further conclusions.

Figure 2 demonstrates the variations in the intensity of cosmic rays with the year of their arrival for the above-mentioned energy intervals. Spectra (a) and (b) correspond only to those showers whose axes have fallen within the central circle of the array with radius $R \leq 500$ m, and spectra (c) and (d) are for $R \leq 1700$ m. The spectra were detected with an efficiency of ~1. This was provided by the requirement that at least one master triangle ("master") include stations that detected ≥8 particles. While analyzing EASs, the number and

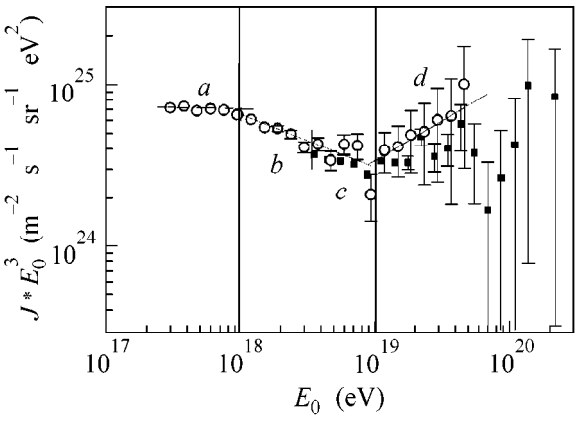

Fig. 1. Energy spectra of ultrahigh energy cosmic rays: (○) Yakutsk data [10]. The lines are the power-law curves fitted to the experimental points with the following parameters in different energy intervals: (*a*) $E_0 < 10^{18}$ eV ($\gamma_a = -3.05 \pm 0.04$), (*b*, *c*) $10^{18} \le E_0 < 10^{19}$ eV ($\gamma_{bc} = -3.34 \pm 0.05$), and (*d*) $E_0 \ge 10^{19.0}$ eV ($\gamma_d = -2.53 \pm 0.25$). (■) AGASA data [11].

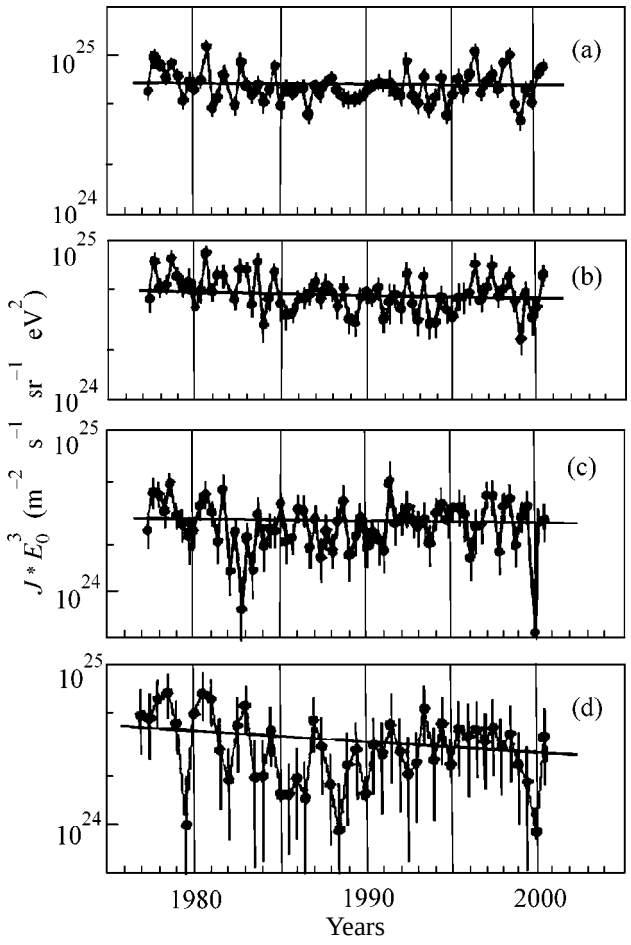

Fig. 2. Yakutsk EAS array data on the intensity of cosmic rays vs. the year of their arrival for different energy intervals: (a) $E_0 < 10^{18}$ eV (6684 showers), (b) $10^{18} \le E_0 < 3 \times 10^{18}$ eV (3253 showers), (c) $3 \times 10^{18} \le E_0 < 10^{19}$ eV (1331 showers), and (d) $E_0 \ge 10^{19}$ eV (214 showers); (●) are the experimental data, and the straight lines are their linear approximations.

configuration of the masters did not change. The events with $E_0 \le 3 \times 10^{18}$ eV were sampled by seven stations forming, together with the central station, six masters with 500-m sides, and the remaining events were sampled by 24 master triangles with 1000-m sides.

The lines in Fig. 2 are linear approximations of the sampled data. One can see that the mean flux of cosmic rays with $E_0 \le 10^{18}$ eV did not change during the indicated time period. Some points (local intensities for 2–3 months) differ ~1.5 times from the mean and often deviate by (3–4)σ. The scatter between the mean minimum and maximum levels is $\Delta J \approx 1.5$.

In the $10^{18} \le E_0 \le 10^{19}$ eV interval, the primary particle flux also was almost unchanged, although there is a hint of its decrease. The scatter of local intensities in Fig. 2b increased to $\Delta J \approx 2$ and, in Fig. 2c, to $\Delta J \approx 2.5$. Many points in Fig. 2b again deviate from the mean by (3–4)σ. Spectra (a) and (b) strongly correlate with each other in shape, with the chance coincidence probability $P < 10^{-5}$. The points themselves deviate from the linear approximations beyond the random scatter ($P < 10^{-5}$).

At $E_0 \ge 10^{19}$ eV, the intensities steadily decline following the linear law (with the rate $\Delta \log J / \Delta T = 0.008 \pm 0.004$ per year). Moreover, a dip with relative (1.5–2)-fold decrease in the EAS arrival frequency was observed from 1982 to 1987. This is clearly seen in Fig. 3a, where each point corresponds to the average annual intensity of events with $E_0 \ge 8 \times 10^{18}$ eV and $\cos\theta \ge 0.6$ falling within the central circle of the array with radius ≤1900 m. The deviations of 24 indications from linear approximation give $\chi^2 = 43.6$ with the chance probability $P \approx 10^{-2}$. Smoothing out these points by linear splines (on ±3 neighboring events) gives the dashed line ($\chi^2 = 28.2$). Within error, this curve does not contradict the experiment ($P \approx 0.24$).

The intensity variations shown in Fig. 2 are not caused by the operating conditions of the Yakutsk array or by the methods of sampling or shower processing. To rule out the most incredible assumption, the average annual Wolf numbers are presented in Fig. 3b [12]. They indicate that the solar cycles have no effect on our results (maybe, due to hypothetical and unknown mechanisms).

The observed features of the EAS arrival frequency have some physical origin. Comparing the data in Fig. 1 with those in Fig. 2, one can assume the following. The events with $E_0 \le (3–5) \times 10^{18}$ eV are likely generated in the Galaxy. Their global flux over a long period of time (tens of years), most likely, remains

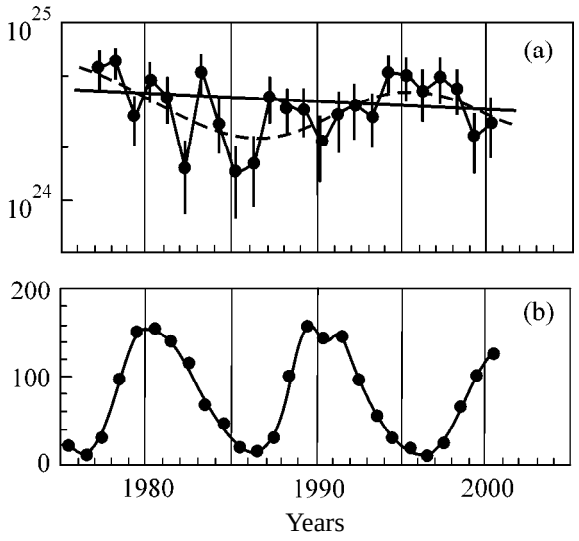

Fig. 3. (a) Intensity of cosmic rays vs. the year of their arrival for $E_0 \geq 8 \times 10^{18}$ eV (287 showers); the straight line is linear approximation of the data and the dashed line is their approximation by linear splines on ±3 neighboring points. (b) Average annual Wolf numbers [12].

unchanged. To draw more definite conclusions, the range of observations should be extended (e.g., doubled). As to the local (1–2 years) intensity variations, they may be due to the varying conditions for the travel of ultrahigh energy cosmic rays.

In all likelihood, cosmic rays with energies $E_0 \geq (8–10) \times 10^{18}$ eV have mostly the extragalactic origin. This is evidenced by the correlations between the positions of a "knee" in Fig. 1 and the North–South asymmetry (with an excess in the southern direction) about the galactic plane in the arrival direction of the particles with these energies [7]. More recently, it has been found [8, 9] that this excess arrives from the direction of the supergalactic plane and has a variable intensity [9]. Figure 3a demonstrates new details of its time-unstable character. It is not improbable that the linear decrease during the period from 1977 to 2000 is only a part of some long-time (hundreds of years) intensity variations (periodic or stochastic) of cosmic rays with the indicated energies. These variations are superposed by other shorter time ones (dashed line in Fig. 3a). Their origin may only be the subject of speculations. The observations should be continued. In this respect, the data of other world EAS arrays are of great interest.

CONCLUSION

It follows from the data presented in this work that additional information on the primary particles may be gained from the "anisotropy" of the time of their arrival. The study of this anisotropy may be helpful in solving the problem of origin of the highest energy cosmic rays. Our data indicate that their intensity is variable. It is still hard to tell by which processes (generation or traveling conditions) they are caused. The intensities show a steady decrease at $E_0 \geq 10^{19}$ eV. A comparison of the energy spectra of cosmic rays measured at different times may lead to erroneous conclusions unless this fact is taken into account.

This work was supported by the Ministry of Sciences of Russian Federation (support for the Yakutsk complex EAS array included under no. 01-30 into the Register of the Unique Research and Experimental Instruments of National Significance).

REFERENCES

1. A. V. Glushkov, V. B. Kosarev, I. T. Makarov, *et al.*, Pis'ma Zh. Éksp. Teor. Fiz. **67**, 361 (1998) [JETP Lett. **67**, 383 (1998)].
2. A. V. Glushkov, I. T. Makarov, M. I. Pravdin, *et al.*, Pis'ma Zh. Éksp. Teor. Fiz. **71**, 145 (2000) [JETP Lett. **71**, 97 (2000)].
3. A. V. Glushkov, M. I. Pravdin, I. E. Sleptsov, *et al.*, Yad. Fiz. **63**, 1557 (2000) [Phys. At. Nucl. **63**, 1477 (2000)].
4. A. A. Mikhailov, in *Proceedings of the 26th International Cosmic Ray Conference, 1999*, Vol. 3, p. 268.
5. M. Takeda, N. Hayashida, K. Honda, *et al.*, Astrophys. J. **522**, 225 (1999).
6. J. Szabelsky, J. Wdowczyk, and A. W. Wolfendale, J. Phys. G **12**, 1433 (1986).
7. B. N. Afanasiev, M. N. Dyakonov, T. A. Egorov, *et al.*, in *Proceedings of the 24th International Cosmic Ray Conference, 1995*, Vol. 2, p. 756.
8. T. Stanev *et al.*, Phys. Rev. Lett. **75**, 3056 (1995).
9. A. V. Glushkov and I. E. Sleptsov, Izv. Ross. Akad. Nauk, Ser. Fiz. (2001) (in press).
10. M. I. Pravdin, M. N. Dyakonov, A. V. Glushkov, *et al.*, in *Proceedings of the 26th International Cosmic Ray Conference, 1999*, Vol. 3, p. 292.
11. M. Takeda, N. Hayashida, K. Honda, *et al.*, Phys. Rev. Lett. **81**, 1163 (1998).
12. http://sidc.oma.be/html/sunspot.html.

Translated by V. Sakun

JETP Letters, Vol. 73, No. 3, 2001, pp. 118–120. From Pis'ma v Zhurnal Éksperimental'noĭ i Teoreticheskoĭ Fiziki, Vol. 73, No. 3, 2001, pp. 134–136.

Multiple Two-Photon Resonance-Enhanced Ionization of Elements under Natural Conditions: Nebulae in the Vicinity of Hot Stars[1]

S. Johansson and V. S. Letokhov*

Department of Physics, Lund University, Lund, S-221, Sweden

** Institute of Spectroscopy, Russian Academy of Sciences, Troitsk, Moscow region, 142190 Russia*

Received November 24, 2000; in final form, January 9, 2001

The possibility is considered of two-photon ionization of atomic particles, with the atomic (ion) level quantum being in quasi-resonance with an intense incoherent monochromatic VUV light under natural conditions, for example, inside planetary nebulae in the vicinity of bright stars. The collisionless resonance-enhanced photoionization mechanism considered may give rise to multiply charged ions as a result of successive (multiple) resonance-enhanced ionization of the photoions produced in a rarefied media with a very low rate of recombination. © *2001 MAIK "Nauka/Interperiodica".*

PACS numbers: 98.38.Ly; 98.38Bn; 32.80.Rm; 95.30.Dr

Although two-photon absorption was predicted by Göppert-Mayer [l] as far back as 1931, its experimental observation occurred only 30 years later [2] following the invention of laser sources of intense coherent light that led to the discovery of numerous nonlinear optical effects. Almost all of them use not only the high intensity of laser light, but also its coherence that makes it possible to accumulate nonlinear effects, specifically, to generate optical harmonics [3], etc., under conditions of phase matching. Two-photon absorption, however, requires no light coherence, but substantially increases under conditions where quasi-resonance exists with some intermediate quantum level. This allows such an effect to become observable in the case of two-photon ionization, provided that the produced ions accumulate. It is precisely this condition that can be satisfied in the rarefied medium of gas nebulae in space, where the recombination rate of the produced ions is extremely low (10^{-5}–10^{-8} s^{-1}) and where, at the same time, an intense VUV radiation exists at resonance transitions in hydrogen and helium.

Planetary nebulae are known to borrow energy from the star(s) immersed within them. A specific feature of planetary nebulae is a huge optical thickness at the spectral lines of transitions to the ground or metastable states. Because of this, the photons resulting from the recombination of the photoions HII (or HeII), which are constantly produced under the effect of the ionizing radiation of the stars, repeatedly undergo resonance scattering before they leave the nebular media and thus become observable. This diffusive confinement (or trapping) effect is accompanied by the broadening of the emission line and an increase in the radiation intensity inside the nebula, and it is limited either by the decay of photons as a result of absorption or by their escape from the spectral line because of the Doppler frequency redistribution upon their scattering by moving resonant particles [4]. These effects are most important where the optical thickness $\tau_0 \gtrsim (\Delta\omega_{Doop}/2\Gamma)^2$, where $\Delta\omega_{Doop}$ and 2Γ are the Doppler and radiative spectral line widths, respectively, because in this case the trapping effect of the Lorentzian wings of the radiative spectral contour becomes substantial. As a result, the intensity P of the trapped spectral lines reaches its maximum, i.e., the blackbody radiation intensity at the corresponding wavelength λ, and can be described in terms of the effective temperature T_{eff} [4]:

$$I(\lambda, T) = \frac{8\pi}{\lambda^2}\frac{\delta\nu}{(e^{kT_{eff}/h\nu} - 1)}\ [\text{photons}/(\text{cm}^2\ \text{s})], \quad (1)$$

where $\delta\nu$ is the spectral line width (in Hz). For example, for Ly_αHII (λ = 1215 Å) at $T_{eff} = 15 \times 10^3$ K and $\delta\nu \cong 250$ cm^{-1}, the intensity $I \cong 6 \times 10^{20}$ photon/cm^2 s, which corresponds to 10^3 W/cm^2 of CW VUV radiation, a figure as yet unattainable, the present-day laser technology status being what it is. So high a radiation

[1] This article was submitted by the authors in English.

intensity for a comparatively small occupation number of the photon quantum state $\langle n\rangle \cong 5\times 10^{-4}$ is explained by the large number of free-space states within the limits of a solid angle of 4π steradians and the large spectral width $\delta\nu$.

The high intensities of the incoherent but relatively monochromatic radiation (as compared to blackbody radiation) originating inside nebulae are quite sufficient to give rise to such nonlinear effects without requirement of spatial coherence of the radiation or the corresponding phase matching. The relative monochromaticity of the trapped radiation is especially favorable to the nonlinear effects that are sensitive to resonance with the radiation frequency. The accidental resonance effect was already successfully used by Bowen [5] to explain the abnormally bright OIII lines as resulting from their photoselective excitation by the intense OIII line of Ly_αHeII. However, such a one-photon resonance excitation requires that the atomic transition be in exact resonance with the photon frequency, since the energy difference cannot be transferred to some third partner in very rarefied nebular media (Fig. 1a). This mechanism proves to be effective where the transfer radiation broadening can provide the necessary resonance with the absorption line. The situation with resonance-enhanced two-photon transition to the ionization continuum (Fig. 1b) is more favorable. In this case, the energy difference $h\Delta\nu$ may be much greater than $h\delta\nu$, because it is offset by the change in the kinetic energy of electrons upon their bound–free transitions through intermediate virtual states to the ionization continuum. When the frequency detuning $\Delta\nu$ is much greater than $\delta\nu$, the two-photon rate (in s^{-1}) is expressed as

$$W_{ph}^{(2)} \cong \frac{1}{32\pi^3}\frac{g_2\lambda^2\sigma_{2i}}{g_1(\Delta\nu)^2}A_{21}I^2, \qquad (2)$$

where σ_{2i} is the cross section for photoionization from the real excited state *2* at a wavelength of λ and g_i is the statistical weight of the *i*th level. A_{21} is the Einstein coefficient for the *1–2* transition. $\Delta\nu \gg \delta\nu$ is the detuning of the radiation frequency with respect to the exact resonance frequency (in Hz), and the intensity I of the isotropic radiation within the spectral width $\delta\nu$ is defined by Eq. (1). If the energy of photons of the same frequency $h\nu$ is not sufficient to photoionize the excited state, the second step of the two-photon process can quite well be effected by photons of higher energies associated with other trapped lines, such as HeI and HeII (Fig. 1c). In this case, the two-color two-photon process will be effected by the bichromatic isotropic radiation of two trapped spectral lines at frequencies ν_i and with spectral widths $\delta\nu_i$, intensities I_i defined by Eq. (1), and effective temperatures $T_{\rm eff}$. The rate of the two-color two-photon process is described as before by Eq. (2), wherein the product I_1I_2 is substituted by I^2.

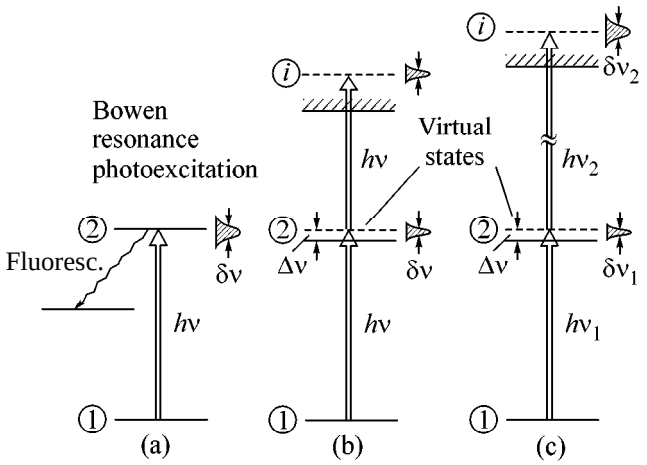

Fig. 1. (a) Resonance fluorescence excitation by the Bowen mechanism and various scheme of (b) one-color and (c) two-color resonance-enhanced two-photon ionization.

For a typical case of Ly_αHI at $\sigma_{2i} \cong 10^{-17}$ cm^2 and $A_{21} \cong 10^9$ s^{-1} and a spectral width of $\delta\nu \cong 300$ cm^{-1} and $\Delta\nu \cong 1000$ cm^{-1}, the rate $W_{ph}^{(2)}$ at $T_{\rm eff} \cong 15\times 10^3$ K reaches 10^{-7} s^{-1}. This value is very small for laboratory experiments [6], but is quite substantial under nebular conditions, wherein the recombination rate $W_{\rm rec}$ is very low. At $W_{ph}^{(2)} > W_{\rm rec}$, the accumulation of photoions of the next ionization degrees takes place. As an illustration, Fig. 2 presents a chain of successive (multiple) two-photon resonance-enhanced ionization schemes for carbon atoms up to multicharged ions CV exposed to intense lines of HI, HeI, and HeII. Similar multiple ionization schemes are also valid for NI $\longrightarrow$ NV, OI $\longrightarrow$ OV, NeI $\longrightarrow$ NeV, and ArI $\longrightarrow$ ArVI, which will be discussed in a separate publication in a specialized journal.

In addition, $W_{ph}^{(2)}$ can perceptibly exceed the collisional electron ionization rate W_e, and this will intensify the corresponding recombination lines that are frequently interpreted within the framework of the electron ionization mechanism as being the result of an anomalous abundance of the element.

We would like to emphasize in conclusion that the two-photon ionization is a purely photonic mechanism that requires no collisions. For this reason, it is especially effective under conditions of space with low electron concentrations, whose extent is large enough to form strong optically thick emission spectral lines of HI, HeI, and HeII. The manifestations of the above mechanism in the emission spectra of nebulae will be discussed in detail in a special astrophysical journal. In this paper, we have restricted ourselves to the consideration of the manifestation of the *nonlinear optical effect under natural conditions*. It should be noted that

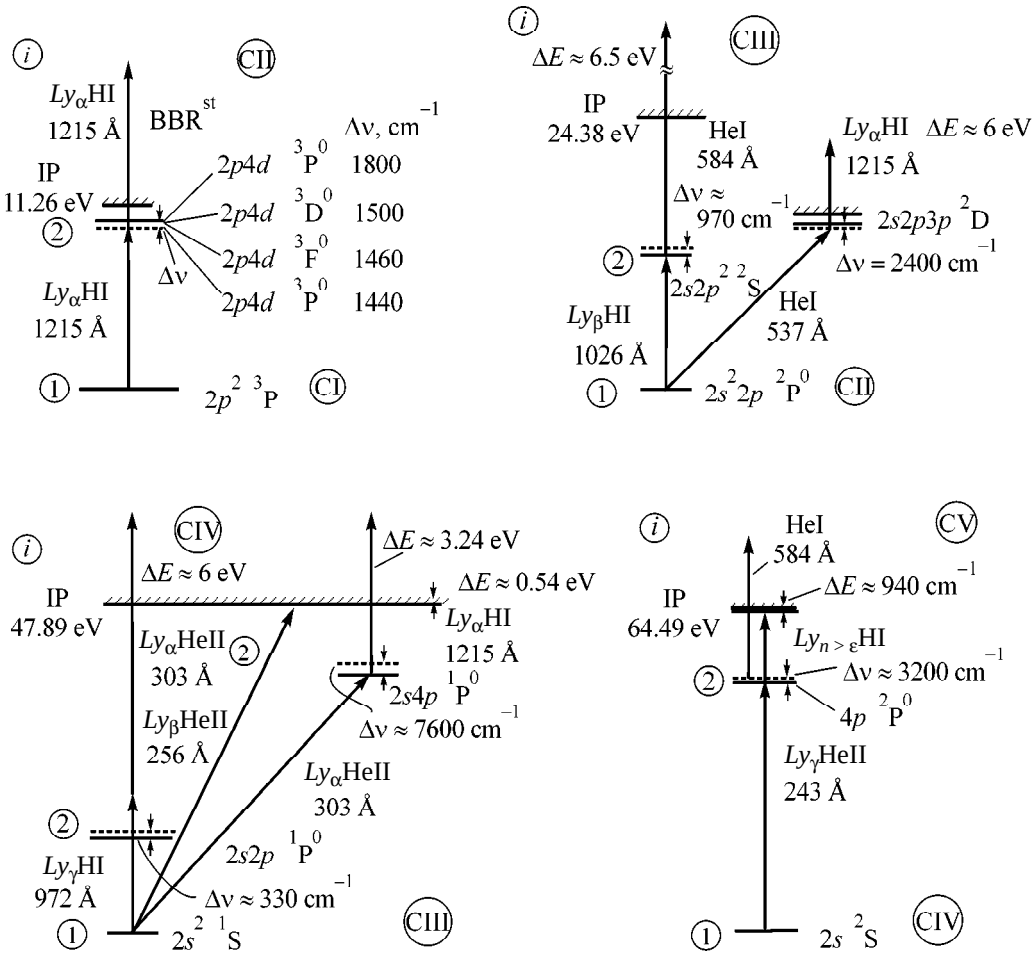

Fig. 2. Schemes of the successive (multiple) resonance-enhanced two-photon ionization of carbon atoms and ions up to CV by intense lines of HI, HeI, and HeII.

the possibility of nonlinear optical effects occurring under astrophysical conditions, specifically in stellar atmospheres, was generally discussed by Vavilov [7] as far back as 1950.

One of us (V.S.L.) is grateful to Dr. A. A. Makarov for useful discussion of the problem.

REFERENCES

1. M. Göppert-Mayer, Ann. Phys. (Leipzig) **9**, 273 (1931).
2. W. Kaiser and C. G. B. Garret, Phys. Rev. Lett. **7**, 229 (1961).
3. P. A. Franken, A. E. Hill, C. W. Peters, and G. Weinreich, Phys. Rev. Lett. **7**, 118 (1961).
4. D. E. Osterbrock, *Astrophysics of Gaseous Nebulae and Active Galactic Nuclei* (University Science Books, Sausalito, 1989).
5. I. S. Bowen, Astrophys. J. **81**, 1 (1935).
6. V. S. Letokhov, *Laser Photoionization Spectroscopy* (Academic, Orlando, 1987).
7. S. I. Vavilov, *Microstructure of Light* (Akad. Nauk SSSR, Moscow, 1950).

JETP Letters, Vol. 73, No. 3, 2001, pp. 121–125. Translated from Pis'ma v Zhurnal Éksperimental'noĭ i Teoreticheskoĭ Fiziki, Vol. 73, No. 3, 2001, pp. 137–142.

Magnetic Catalysis of *P*-Parity Breakdown in a Massive Gross–Neveu Model and High-T_c Superconductivity

V. Ch. Zhukovskiĭ[1], K. G. Klimenko[2], V. V. Khudyakov[1], and D. Ébert[3]

[1] *Moscow State University, Vorob'evy gory, Moscow, 119899 Russia*

[2] *Institute for High Energy Physics, Protvino, Moscow region, 142284 Russia*

[3] *Research Center for Nuclear Physics, Osaka University, Ibaraki, Osaka 567, Japan, and Insitut für Physik, Humboldt Universität zu Berlin, D-10115 Berlin, Germany*

Received December 25, 2000

It is shown within the framework of the (2 + 1)-dimensional *P*-invariant massive Gross–Neveu theory that an external magnetic field induces a first-order phase transition that breaks the *P* parity. The use of the obtained results in the description of magnetic phase transitions in high-T_c superconductors is discussed. © *2001 MAIK "Nauka/Interperiodica"*.

PACS numbers: 74.20.-z; 74.25.Nf; 11.10.Kk; 11.30.Rd

Dynamical symmetry breaking induced by external (chromo)magnetic fields is called magnetic catalysis. Gross and Neveu [1] were the first to observe this property of an external uniform magnetic field H in studying the (2 + 1)-dimensional (three-dimensional) chiral-invariant field theory with four-fermion interaction. In these theories, which are also referred to as Gross–Neveu (GN) theories, an infinitesimal external magnetic field leads to dynamical chiral symmetry breaking (DCSB) even if the coupling constant is as small as one likes [2, 3]. This phenomenon was later attributed to the effective reduction of the space–time dimension in an external magnetic field and, correspondingly, to the increased role of infrared divergences in the vacuum rearrangement [4]. More recently, it was shown that DCSB is also induced by an external chromomagnetic field [5–7]. Moreover, Semenoff *et al.* [8] have examined a number of theories and pointed out that magnetic catalysis of DCSB is possibly model-independent. Gusynin *et al.* [4] proved this statement for three-dimensional theories. Liu [9] showed recently for the three-dimensional *P*-invariant GN model that the external magnetic field is also a catalyst for spontaneous *P*-parity breakdown. Magnetic catalysis was already used in the cosmological and astrophysical studies [10] and in the construction of the theory of high-T_c superconductivity [9, 11–13]. It is safe to say that this effect will find use in the future in particle physics, physics of condensed matter, neutron star physics, etc., i.e., in the fields of science where dynamical symmetry breaking is of fundamental importance and the external magnetic field is an objective reality.[1]

Considerable interest shown in the last decade in three-dimensional field theories, including GN models [15], is largely explained by the fact that high-T_c superconductivity (HTSC) has a planar character because conduction electrons in the HTSC systems are concentrated in the planes formed by the Cu and O atoms [16]. It was found in a recent experiment [17] with $Bi_2Sr_2CaCu_2O_8$ HTSC that the heat conductivity as a function of the external magnetic field H changes abruptly at a certain value $H = H_c \sim T^2$ (sample temperature $T < T_c$, where T_c is the temperature of superconducting transition). The authors of [17] assumed that the external magnetic field induces phase transition at $H = H_c$. Shortly after, Laughlin [18] used the free-energy functional formalism to suggest a phenomenological description of this phase transition as a first-order phase transition with *P*-parity breakdown. In addition, Liu [9] and Semenoff *et al.* [11] have proposed theoretical (microscopic) explanations of this phenomenon within the framework of two three-dimensional GN models based on magnetic catalysis of dynamical symmetry breaking.[2] In one of them, the magnetic field induces DCSB [11], and, in another, *P*-parity breakdown occurs [9]. In both models, the phase transitions are continuous. In other words, both chiral symmetry in [11] and *P* symmetry in [9] break at $H = H_c$ in the second-order phase transition, in conflict with the phenomenological approach [18].

It is shown in this work that a (2 + 1)-dimensional GN model exists in which the qualitative features of

[1] Possible applications of magnetic catalysis are also discussed in [14].

[2] Recently, the possibility of describing this phase transition by other three-dimensional relativistic theories was also discussed [19].

magnetic catalysis are the same as in the phenomenological description [18] of the phase transition induced by an external magnetic field in HTSC systems.

We consider the effect of an external magnetic field on the phase structure of a (2 + 1)-dimensional GN model with the Lagrangian

$$L = \sum_{a=1}^{N} (\bar{\psi}_a i\hat{\partial}\psi_a + m\bar{\psi}_a\psi_a) + \frac{G}{2N}\left(\sum_{a=1}^{N}\bar{\psi}_a\tau\psi_a\right)^2, \quad (1)$$

where $\hat{\partial} \equiv \gamma^\mu\partial_\mu$, and the fields ψ_a form the basis of a fundamental representation of the $U(N)$ group, which is introduced in order to use the nonperturbative $1/N$ expansion in the calculations. The Fermi fields ψ_a for each $a = 1, 2, \ldots, N$ are four-component Dirac spinors (the corresponding indices are omitted) reducible in the Lorentz group, and $\tau = \mathrm{diag}(1, 1, -1, -1)$ is the matrix in the spinor space. The action corresponding to Lagrangian (1) is invariant under the discrete P-parity transformation: $\psi_a(t, x, y) \longrightarrow i\gamma^1\gamma^5\psi_a(t, -x, y)$ (the algebra of γ^μ matrices for the reducible four-dimensional spinor representation of Lorentz group in the three-dimensional space was presented in [20]). It is this model which was used (with $m = 0$) in [9] to describe the phase transitions induced by an external magnetic field in HTSC systems.

We demonstrate that, in contrast to the $m = 0$ case, the external magnetic field in the model with $m \neq 0$ induces dynamical P-parity breakdown at the critical point $H = H_c$. The breakdown is discrete, i.e., corresponding to a first-order phase transition. This feature of magnetic catalysis in model (1) with $m \neq 0$ has no analogues in other models of field theory. The obtained results allow us to believe that the magnetic phase transition observed in experiment [17] can be theoretically explained by means of massive GN model (1) and in agreement with the phenomenological approach [18].

1. Phase structure of the model at $H = 0$. Before analyzing the effect of a nonzero external magnetic field H on the vacuum of model (1), we examine its phase structure at $H = 0$. To this end, let us introduce an auxiliary Lagrangian of the form

$$\tilde{L} = \bar{\psi}i\hat{\partial}\psi + m\bar{\psi}\psi + \sigma\bar{\psi}\tau\psi + N\sigma^2/2G, \quad (2)$$

where $\sigma(x)$ is the auxiliary real boson field and the summation index a for the auxiliary $U(N)$ group is hereafter implied. Field theories (1) and (2) are mutually equivalent because the field σ can be excluded from Eq. (2) by using the equations of motion to obtain Lagrangian (1). It is easy to show that the auxiliary field is transformed as $\sigma(t, x, y) \longrightarrow -\sigma(t, -x, y)$ under the discrete P-parity operation; i.e., σ is a pseudoscalar field. Using Lagrangian (2), one can find the effective potential, which has the following form in the one-loop approximation, i.e., in the leading order of the $1/N$ expansion:

$$V_0(\sigma) = \frac{N\sigma^2}{2G} - N\sum_{k=1}^{2}\int\frac{d^3p}{(2\pi)^3}\ln(p^2 + M_k^2), \quad (3)$$

where the integration goes over the Euclidean momentum space and $M_{1,2} = |m \pm \sigma|$. Integration in Eq. (3) over the region $0 \le p^2 \le \Lambda^2$ gives

$$\frac{1}{N}V_0(\sigma) = \frac{\sigma^2}{2g} + \frac{|m-\sigma|^3}{6\pi} + \frac{|m+\sigma|^3}{6\pi}, \quad (4)$$

where $1/g = 1/G - 2\Lambda/\pi^2$. It is known that the phase structure of any field theory is to a great extent determined by the symmetry properties at the global-minimum point of its effective potential. One can easily show that the point $\sigma = 0$ symmetric about the P-parity transformation corresponds to the global minimum of function (4) for $\pi/g > -2m$. If $\pi/g < -2m$, then potential (4) has the absolute minimum at a nonzero point on the set $0 \le \sigma \le \infty$

$$\sigma_0 = -\frac{\pi}{2g} + \sqrt{\frac{\pi^2}{4g^2} - m^2} \quad (5)$$

and the P symmetry of the model spontaneously breaks. By using the bare coupling constant G instead of g, one can arrive at the following conclusions. For $G < G_c = \pi^2/(2\Lambda - 2m\pi)$, the vacuum of the model is P-invariant, and for $G > G_c$ the phase with spontaneous P-symmetry breaking is realized. The first-order phase transition occurs at the point $G = G_c$ because the global minimum of the potential moves jumpwise from the origin of coordinates to nonzero point (5). Note for comparison that in a massless model, i.e., for $m = 0$, the system undergoes a second-order phase transition at the point $G = G_c$ with continuously changing coupling constant.

2. Magnetic catalysis of dynamical P-parity breakdown. Let us now analyze how the external magnetic field H (zero temperature) affects the symmetric phase of model (1); i.e., $\pi/g > -2m$ (the bare coupling constant is small, $G < G_c$). The corresponding effective potential, which is a special case of the effective potential in a more general GN model with $H \neq 0$ [20], has the form

$$V_H(\sigma) = \frac{N\sigma^2}{2g} + N\sum_{k=1}^{2}\left[\frac{eHM_k}{4\pi} - \frac{(2eH)^{3/2}}{4\pi}\zeta\left(-\frac{1}{2}, \frac{M_k^2}{2eH}\right)\right], \quad (6)$$

where $\zeta(s, x)$ is the generalized Riemann zeta function [21]. Let us show that the external magnetic field induces spontaneous P-parity breakdown for the model

(magnetic catalysis) and that the character of this phenomenon is qualitatively different for $m = 0$ and $m \neq 0$.

Case $m = 0$. The effective potential $V_H^{m=0}(\sigma)$ of the model is obtained from Eq. (6) by setting $m = 0$:

$$V_H^{m=0}(\sigma) = \frac{N\sigma^2}{2g} + \frac{NeH|\sigma|}{2\pi} - \frac{N(2eH)^{3/2}}{2\pi}\zeta\left(-\frac{1}{2}, \frac{\sigma^2}{2eH}\right). \quad (7)$$

The function $V_H^{m=0}(\sigma)$ is, clearly, symmetric about the transformation $\sigma \longrightarrow -\sigma$. Therefore, to find the global-minimum point, it is sufficient to analyze it only on the set $\sigma \in [0, \infty)$. In this case, the stationarity equation

$$\frac{\partial V_H^{m=0}(\sigma)}{\partial\sigma} \equiv 2N\sigma F(\sigma) = 2N\sigma\left[\frac{1}{2g} + \frac{eH}{4\pi\sigma} - \frac{\sqrt{2eH}}{4\pi}\zeta\left(\frac{1}{2}, \frac{\sigma^2}{2eH}\right)\right] = 0 \quad (8)$$

is derived from Eq. (7) by using the formula $d\zeta(s, x)/dx = -s\zeta(s + 1, x)$. Although potential (7) has already been analyzed in [2, 4, 6], we present here some details that are important in further consideration.

First of all, it follows from Eq. (8) that

$$\left.\frac{\partial V_H^{m=0}(\sigma)}{\partial\sigma}\right|_{\sigma\to 0_+} = \lim_{\sigma\to 0_+}(2N\sigma F(\sigma)) = -\frac{NeH}{2\pi}; \quad (9)$$

i.e., the point $\sigma = 0$ is not a solution of stationarity equation (8). In addition, since $V_H^{m=0}(\sigma) = V_H^{m=0}(-\sigma)$, Eq. (9) has two more consequences: (i) the point $\sigma = 0$ is a local minimum of the potential, and (ii) the first derivative of the function $V_H^{m=0}(\sigma)$ does not exist at the point $\sigma = 0$. At the same time, the effective potential for $H = 0$ is a function differentiable over the entire σ axis. Consequence (i) and the fact that $\lim_{|\sigma|\to\infty} V_H^{m=0}(\sigma) = +\infty$ indicate that the potential $V_H^{m=0}(\sigma)$ has a nonzero global-minimum point $\sigma_0(H)$. This means that the *P* symmetry of the massless model under consideration is necessarily spontaneously broken in the presence of an infinitesimal external magnetic field even if the coupling constant *G* is as small as one likes (in this case $g > 0$). Thus, the external magnetic field induces dynamical *P*-parity breakdown (magnetic catalysis).

It is known that the function $F(\sigma)$ monotonically increases on the set $\sigma \in [0, \infty)$, so that $F(0) = -\infty$ [it follows from Eq. (9)] and $\lim_{|\sigma|\to\infty} F(\sigma) = \infty$ [2, 6]. Therefore, there is only one point $\sigma_0(H)$ where the function $F(\sigma)$ vanishes, and this point is the global-minimum point of potential (7). From the equation $F(\sigma) = 0$ treated as an equality implicitly defining the function $\sigma_0(H)$, it follows that $\sigma_0(H) \approx egH/(2\pi)$ at $H \longrightarrow 0$ [2, 6].

Thus, switching on a magnetic field in the model induces a *P*-parity-breaking second-order phase transition, which is continuous in *H* because the order parameter $\sigma_0(H)$ is a continuous function of *H* at the point $H = 0$ of phase transition.

It was proved earlier [2, 6] that $\sigma_0(H) \approx k\sqrt{eH}$ at large *H*, where $k \approx 0.45$ is the solution of the equation $\sqrt{2}\,\zeta(1/2, k^2/2) = 1$. Because $\sigma_0(H)$ is the global-minimum point of potential (7), the inequality $V_H^{m=0}(0) > V_H^{m=0}(\sigma_0(H))$ is valid for all *H* values. In particular, by using this inequality for $H \longrightarrow \infty$, we obtain the inequality

$$-\frac{N(2eH)^{3/2}}{2\pi}\zeta\left(-\frac{1}{2}, 0\right) > \frac{Nk(eH)^{3/2}}{2\pi} - \frac{N(2eH)^{3/2}}{2\pi}\zeta\left(-\frac{1}{2}, \frac{k^2}{2}\right). \quad (10)$$

Case $m \neq 0$. Let us now consider some features of spontaneous symmetry breaking in model (1) at *H*, $m \neq 0$. As in the massless case, the potential $V_H(\sigma)$ at $m \neq 0$ is an even function of variable σ. Therefore, it will suffice to examine this potential only on the semiaxis $\sigma \in [0, \infty)$. The corresponding stationarity equation for the effective potential has the form

$$0 = \frac{1}{N}\frac{\partial V_H}{\partial\sigma} = \begin{cases} (\sigma + m)F(\sigma + m) - (m - \sigma)F(m - \sigma) & \text{at } \sigma < m \\ (\sigma + m)F(\sigma + m) + (\sigma - m)F(\sigma - m) & \text{at } \sigma > m, \end{cases} \quad (11)$$

where the function $F(x)$ is given in Eq. (8). Taking Eq. (9) into account, one can easily obtain from Eq. (11) that

$$\left.\frac{\partial V_H}{\partial\sigma}\right|_{\sigma\to m_+} = -\frac{NeH}{2\pi} + \left.\frac{\partial V_H}{\partial\sigma}\right|_{\sigma\to m_-}, \quad (12)$$

which means that potential (6) is not differentiable at the points $\sigma = \pm m$ at $H \neq 0$. For this reason, the global minimum of the function $V_H(\sigma)$ on the set $\sigma \in [0, \infty)$ can occur either at the point $\sigma = m$ or at the point given by one of the solutions of stationarity equation (11). However, using Eq. (12), one can draw the following important conclusion: if the derivative of the effective potential is negative in some left vicinity of the point $\sigma = m$, this derivative is also negative in some right vicinity of this point. Therefore, $\sigma = m$ is not a point of the global, and even a local, minimum, so that we focus on the solutions of Eq. (11).

The point $\sigma = 0$ is the obvious solution of this equation at all *H* values. Using analytical and numerical methods, one can prove that, for all $H \neq 0$, this point

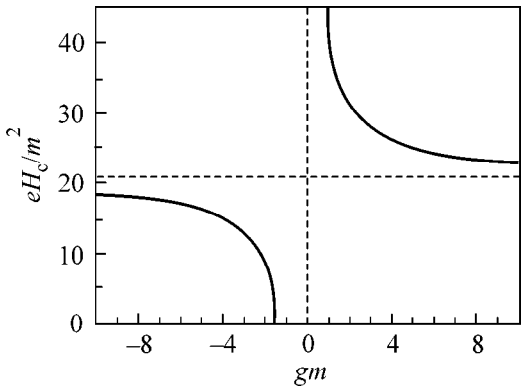

Fig. 1. Critical magnetic field vs. coupling constant g.

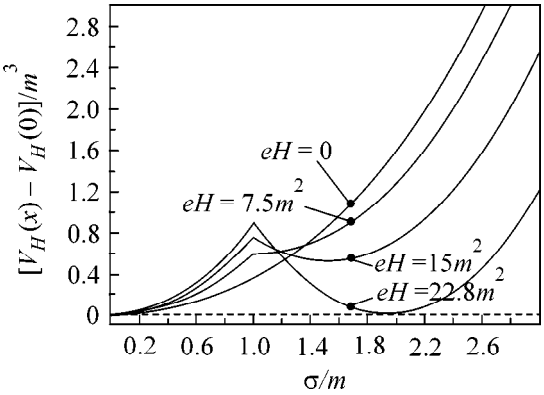

Fig. 2. Effective potential for different values of magnetic field at $gm = 10$.

corresponds at least to a local minimum of the function $V_H(\sigma)$. Moreover, the global potential minimum for small H values occurs at the point $\sigma = 0$ and the P parity remains unbroken [this is due to the fact that the derivative of the potential for these H is positive for all $\sigma \in [0, \infty)$].

Let us show that, at large H, Eq. (11) has one more solution, which is absent for small H. Indeed, in the region $\sigma \gg m$, this equation coincides in form with stationarity equation (8) for the massless case. The solution $\sigma_0(H)$ of the latter becomes large only in the limit $eH \longrightarrow \infty$. Therefore, at large magnetic fields, Eq. (11) has, apart from $\sigma = 0$, one more solution $\tilde{\sigma}_0(H)$ such that $\tilde{\sigma}_0(H) \approx k\sqrt{eH}$ at $eH \longrightarrow \infty$, where the coefficient k is the same as in Eq. (10). We failed to find solutions of stationary equation (11) other than $\sigma = 0$ and $\tilde{\sigma}_0(H)$.

As was mentioned above, the global potential minimum for small H values occurs at the point $\sigma = 0$. Let us show that this minimum moves to the point $\tilde{\sigma}_0(H)$ as H increases. At $eH/m^2 \longrightarrow \infty$, the potential at the stationary points takes the values

$$V_H(0) = -\frac{(2eH)^{3/2}}{2\pi}\zeta\left(-\frac{1}{2}, 0\right) + O(eH/m^2), \quad (13)$$

$$V_H(\tilde{\sigma}_0(H)) = \frac{k(2eH)^{3/2}}{2\pi} - \frac{(2eH)^{3/2}}{2\pi}\zeta\left(-\frac{1}{2}, \frac{k^2}{2}\right) + O(eH/m^2), \quad (14)$$

where it is taken into account that $\bar{\sigma}_0(H) \approx k\sqrt{eH}$ at $eH \longrightarrow \infty$. A comparison of Eqs. (13) and (14), with regard to Eq. (10), gives $V_H(\tilde{\sigma}_0(H)) < V_H(0)$ at $eH \longrightarrow \infty$. Since for all H values $\sigma = 0$ is at least a local-minimum point, the global minimum of the potential moves jumpwise from the point $\sigma = 0$ to the nontrivial point $\tilde{\sigma}_0(H)$ at a certain critical value of external magnetic field $H_c(g) \neq 0$. Thus, the point $H_c(g)$ is the point of a P-parity-breaking first-order phase transition. Figure 1 shows the critical magnetic field $H_c(g)$ as a function of the g constant at $T = 0$ and $m \neq 0$. Figure 2 presents the function $V_H(\sigma)$ for various H values at $gm = 10$.

3. Magnetic catalysis at nonzero temperature *T*. Using the technique developed in [4], one can obtain the following expression for the effective potential of model (1) at $H, T \neq 0$:

$$\frac{1}{N}V_{HT}(\sigma) = \frac{1}{N}V_H(\sigma) - \frac{eH}{2\pi\beta}\sum_{i=1}^{2}\left\{\ln(1 + \exp(-M_i\beta)) + 2\sum_{k=1}^{\infty}\ln(1 + \exp(-\beta\sqrt{M_i^2 + 2keH}))\right\}, \quad (15)$$

where $\beta = 1/T$ and $V_H(\sigma)$ is potential (6). Numerical analysis of potential (15) shows that the parity is also not broken at small H values. However, at some critical magnetic field, the P-parity-breaking first-order phase transition occurs. Let us denote the critical field at a fixed g value by $H_c(T)$. Some of its values are given in the table for $gm = 5$. One can see from the table that $H_c(T) \sim T^2$ at $T \longrightarrow \infty$; i.e., the behavior of $H_c(T)$ is the same as in the models [9, 11].

In summary, we have proved, within the framework of the field theory, that an external magnetic field can induce the first-order phase transition.[3] The P-invariant massive three-dimensional GN model (1) is proposed as an example. Magnetic catalysis of dynamical P-symmetry breaking occurs in this model at $m = 0$ [9]. In this case, the second-order phase transition occurs at the point $H_c \sim T^2$ ($T \longrightarrow \infty$) and the theoretical H_c values agree well with experimental data [17].

[3] Recent numerical analysis carried out in the chiral-invariant QED_3 model also indicates that magnetic catalysis of DCSB is possible through the first-order phase transition [13].

$H_c(T)$ values at $gm = 5$

T/m	0.1	0.25	0.5	1	2.5	5	10	25	50	100	200
$eH_c(T)/m^2$	24.9	25.2	27	36	131	465	1782	10900	43200	173000	700000

We have shown that an external magnetic field induces dynamical *P*-parity breakdown in model (1) at $m \neq 0$ as well. The behavior of the H_c curve at large T is the same as for $m = 0$. However, in contrast to the latter case, in massive GN model (1) a *P*-parity-breaking first-order phase transition occurs at the H_c point, in agreement with the phenomenological description [18] of the magnetic phase transitions experimentally observed in the HTSC systems [17].

One of us (D.E.) acknowledges the Japanese Ministry of Education for the support of his work at the Research Center for Nuclear Physics, Osaka University. This study was supported by the Russian Foundation for Basic Research (project no. 98-02-16690) and by the German Research Society (DFG-Project 436 RUS 113/477/4). We are grateful to S. Sachdev for pointing out recent papers [19], where the Gross–Neveu equation was microscopically derived and its relation to the recent experiments was discussed.

REFERENCES

1. D. J. Gross and A. Neveu, Phys. Rev. D **10**, 3235 (1974).
2. K. G. Klimenko, Teor. Mat. Fiz. **89**, 211 (1991); **90**, 3 (1992); K. G. Klimenko, Z. Phys. C **54**, 323 (1992).
3. I. V. Krive and S. A. Naftulin, Phys. Rev. D **46**, 2737 (1992).
4. V. P. Gusynin, V. A. Miransky, and I. A. Shovkovy, Phys. Rev. Lett. **73**, 3499 (1994); Phys. Rev. D **52**, 4718 (1995).
5. K. G. Klimenko, A. S. Vshivtsev, and B. V. Magnitsky, Nuovo Cimento A **107**, 439 (1994); A. S. Vshivtsev, K. G. Klimenko, and B. V. Magnitskiĭ, Teor. Mat. Fiz. **101**, 391 (1994); Yad. Fiz. **57**, 2260 (1994) [Phys. At. Nucl. **57**, 2171 (1994)].
6. A. S. Vshivtsev, V. Ch. Zhukovskiĭ, K. G. Klimenko, and B. V. Magnitskiĭ, Fiz. Élem. Chastits At. Yadra **29**, 1259 (1998) [Phys. Part. Nucl. **29**, 523 (1998)].
7. I. A. Shovkovy and V. M. Turkowski, Phys. Lett. B **367**, 213 (1996); D. Ebert and V. Ch. Zhukovsky, Mod. Phys. Lett. A **12**, 2567 (1997); V. P. Gusynin, D. K. Hong, and I. A. Shovkovy, Phys. Rev. D **57**, 5230 (1998).
8. G. W. Semenoff, I. A. Shovkovy, and L. C. R. Wijewardhana, Phys. Rev. D **60**, 105024 (1999).
9. W. V. Liu, Nucl. Phys. B **556**, 563 (1999).
10. T. Inagaki, T. Muta, and S. D. Odintsov, Prog. Theor. Phys. Suppl. **127**, 93 (1997); E. J. Ferrer and V. de la Incera, Int. J. Mod. Phys. A **14**, 3963 (1999); hep-th/9910035.
11. G. V. Semenoff, I. A. Shovkovy, and L. C. R. Wijewardhana, Mod. Phys. Lett. A **13**, 1143 (1998).
12. K. Farakos and N. E. Mavromatos, Int. J. Mod. Phys. B **12**, 809 (1998); K. Farakos, G. Koutsoumbas, and N. E. Mavromatos, Int. J. Mod. Phys. B **12**, 2475 (1998); N. E. Mavromatos and A. Momen, Mod. Phys. Lett. A **13**, 1765 (1998).
13. J. Alexandre, K. Farakos, and G. Koutsoumbas, hep-th/0010211.
14. V. A. Miransky, Prog. Theor. Phys. Suppl. **123**, 49 (1996); V. P. Gusynin, Ukr. Phys. J. **45** (4/5), 603 (2000); V. de la Incera, hep-ph/0009303.
15. G. W. Semenoff and L. C. R. Wijewardhana, Phys. Rev. Lett. **63**, 2633 (1989); R. Mackenzie, P. K. Panigrahi, and S. Sakhi, Int. J. Mod. Phys. A **9**, 3603 (1994); V. P. Gusynin, V. M. Loktev, and I. A. Shovkovy, Zh. Éksp. Teor. Fiz. **107**, 2007 (1995) [JETP **80**, 1111 (1995)]; E. Babaev, Phys. Lett. B **497**, 323 (2001); hep-th/9909052.
16. A. S. Davydov, Phys. Rep. **190**, 191 (1990).
17. K. Krishana, N. P. Ong, Q. Li, *et al.*, Science **277**, 83 (1997).
18. R. B. Laughlin, Phys. Rev. Lett. **80**, 5188 (1998).
19. M. R. Li, P. J. Hirschfeld, and P. Wolfle, cond-mat/0003160; M. Vojta, Y. Zhang, and S. Sachdev, cond-mat/0003163; cond-mat/0008048; Phys. Rev. Lett. **85**, 4940 (2000); D. V. Khveshchenko and J. Paaske, cond-mat/0009117.
20. V. Ch. Zhukovskiĭ, K. G. Klimenko, and V. V. Khudyakov, Teor. Mat. Fiz. **124**, 323 (2000).
21. E. T. Whittaker and G. N. Watson, *A Course of Modern Analysis* (Cambridge Univ. Press, Cambridge, 1952; Fizmatgiz, Moscow, 1963), Vol. 2.

Translated by R. Tyapaev

JETP Letters, Vol. 73, No. 3, 2001, pp. 126–130. Translated from Pis'ma v Zhurnal Éksperimental'noĭ i Teoreticheskoĭ Fiziki, Vol. 73, No. 3, 2001, pp. 143–147.

Turbulent Transport Processes in a Plasma As a Diffusion Process with Random Time

G. M. Batanov[1], V. E. Bening[2], V. Yu. Korolev[2], A. E. Petrov[1], K. A. Sarksyan[1], N. N. Skvortsova[1], N. K. Kharchev[1], and S. V. Shchepetov[1]

[1] *Institute of General Physics, Russian Academy of Sciences, ul. Vavilova 38, Moscow, 119991 Russia*

[2] *Moscow State University, Vorob'evy gory, Moscow, 119899 Russia*

e-mail: nina@fpl.gpi.ru

Received October 2, 2000; in final form, December 25, 2000

It is proposed to apply the statistical analysis of the increments of fluctuating particle fluxes to analyzing the probability characteristics of turbulent transport processes in plasma. Such an approach makes it possible to analyze the dynamic probability characteristics of the process under study. It is shown that, in the plasmas of the L-2M stellarator and the TAU-1 linear device, the increments of local fluctuating particle fluxes are of stochastic character and that their distributions are scale mixtures of Gaussians. In particular, for TAU-1, the increments have the Laplacian distribution (which is a scale mixture of Gaussians with an exponential mixing distribution). This implies that the rate of flux variations is a diffusion process with random time. It is shown that the characteristic growth (damping) time of fluctuations is one order of magnitude shorter than their characteristic correlation time. Physical mechanisms that may be responsible for the random character of the growth (damping) of fluctuations are discussed. © *2001 MAIK "Nauka/Interperiodica".*

PACS numbers: 52.35.Ra; 52.25.Fi

1. In recent years, the probability characteristics of turbulent transport in plasma, in particular, local fluctuating particle fluxes in a magnetoactive plasma produced both in toroidal and in linear devices have attracted considerable interest [1–3]. However, the authors usually restrict themselves to calculating and describing the characteristics of the probability density function (PDF) of a turbulent particle flux and conclude that the distribution deviates from the Gaussian (normal) distribution. However, mathematical consideration are sometimes insufficiently correct. For example, the conclusion that the PDF differs from Gaussian (in particular, by its higher peakedness) is usually deduced from the shape of the histogram constructed from the values of a local fluctuating particle flux at equidistant times. However, it can be easily shown that, even for a discrete time sequence constructed for the classical process of Brownian motion, this approach gives an excess value of $M_4 \sim 4$ (whereas $M_4 = 3$ for the Gaussian law). Therefore, generally speaking, the assertion about a non-Gaussian character of the original process only by reasoning that the obtained distribution is more peaked (in comparison with the Gaussian law) is obviously incorrect. Until recently, no attempts were made to analyze the mechanisms responsible for the characteristic features of the PDF of fluctuating particle fluxes in plasma. Only recently [4, 5], attempts were made to relate the statistical probability characteristics of fluctuating fluxes to nonlinear wave processes in a plasma.

In this paper, we propose to solve the problem stated above by applying an approach that is widely known in mathematical statistics, first of all, in the analysis of time series (time-dependent stochastic processes), but has not yet been used in plasma physics. In other words, we suggest passing from the statistical analysis of the amplitudes of a fluctuating particle flux to the analysis and modeling of its increments. The reason is that the values of the original process taken at equidistant times do not constitute a homogeneous independent sample, which makes them inappropriate to make decisive conclusions about the statistical probability properties of the process under study. At the same time, the statistical analysis shows that the increments of such a process on noncrossing time intervals always have the same distribution. Therefore, an analysis of the increments of the process can reveal the dynamic characteristics of a fluctuating flux and their relation to certain physical mechanisms.

2. In this paper, we study the probability characteristics of fluctuating particle fluxes measured in the plasmas of the L-2M stellarator and the TAU-1 linear device. The parameters of the devices are presented in [6, 7]. The main distinctions are the magnetic field topology (the L-2M field is toroidal, and the TAU-1 field is uniform) and the electron temperature (T_e =

0.6–1.0 keV in L-2M and T_e = 5–7 eV in TAU-1). Nevertheless, the spectral and statistical plasma characteristics are very similar in both devices [8].

Let us consider the probability characteristics of the local fluctuating particle flux obtained in the course of data processing. We define the local fluctuating particle flux as $\tilde{\Gamma} = (\delta n_e \cdot \delta v_r)$ [2, 3], where δn_e is the plasma density fluctuation, $\delta v_r = \delta E_\Theta / B$ is the radial-velocity fluctuation, $\delta E_\Theta = (\delta\varphi_1 - \delta\varphi_2)/\Delta\Theta r$ is the fluctuation of the poloidal electric field, $\delta\varphi$ is the fluctuation of the plasma floating potential, and Θ is the poloidal angular coordinate. As for the type of instability, the drift-dissipative instability is dominant in TAU-1 [7], whereas the resistive ballooning instability is characteristic of the edge plasma in L-2M [3] and the drift-dissipative instability is typically observed in deeper layers of the stellarator plasma [6]. The frequencies of turbulent fluctuation spectra lie in the range from several kilohertz to one hundred kilohertz for TAU-1 and to several hundred kilohertz for L-2M. Thus for L-2M, the fluctuation spectrum is substantially broader ($\Delta f/f|_{\text{L-2M}} \approx 1$, and $\Delta f/f|_{\text{TAU-1}} \approx 0.3$).

Figure 1 shows typical realizations of a fluctuating flux $\tilde{\Gamma}$ (Fig. 1a) and its increments $\Delta\tilde{\Gamma} = \tilde{\Gamma}_j(t_j) - \tilde{\Gamma}_{j-1}(t_{j-1})$ (Fig. 1b) for the L-2M plasma. As is seen, both signals are intermittent and bursty, which indicates the random nature of both processes. Figure 1c shows the autocorrelation functions (ACF) of the flux and its increments for the same signals. It is seen that, within the time window, the ACF of $\tilde{\Gamma}$ does not attain the noise level, whereas the ACF of $\Delta\tilde{\Gamma}$ attains this level in several microseconds. The slow variation of the ACF of $\tilde{\Gamma}$ demonstrates that the time array of the flux amplitudes does not represent a homogeneous independent sample, whereas the rapid drop in the ACF of $\Delta\tilde{\Gamma}$ indicates the random and independent character of the array of increments (see Section 1). It follows that when applying the conventional methods of probability analysis, it is more correct to use the increments of a fluctuating flux instead of the flux amplitudes.

Figure 2 shows the PDFs for the processes of a local fluctuating particle flux and its increments. The asymmetry coefficient M_3 and the excess coefficient M_4 for the corresponding PDFs are also shown. The PDF of the process $\tilde{\Gamma}$ (Figs. 2a, 2b) demonstrates an appreciable deviation from the Gaussian law, which agrees with what was said in Section 1. What is even more interesting is that the distributions of $\Delta\tilde{\Gamma}$ deviate from Gaussian, while the PDFs themselves are symmetric. The latter circumstance shows that we are dealing with a time-homogeneous process in an open system. In this case, we can speak about the steady-state dynamic process of the growth and damping of a fluctuating flux. A similar picture is also observed for the PDFs of the increments

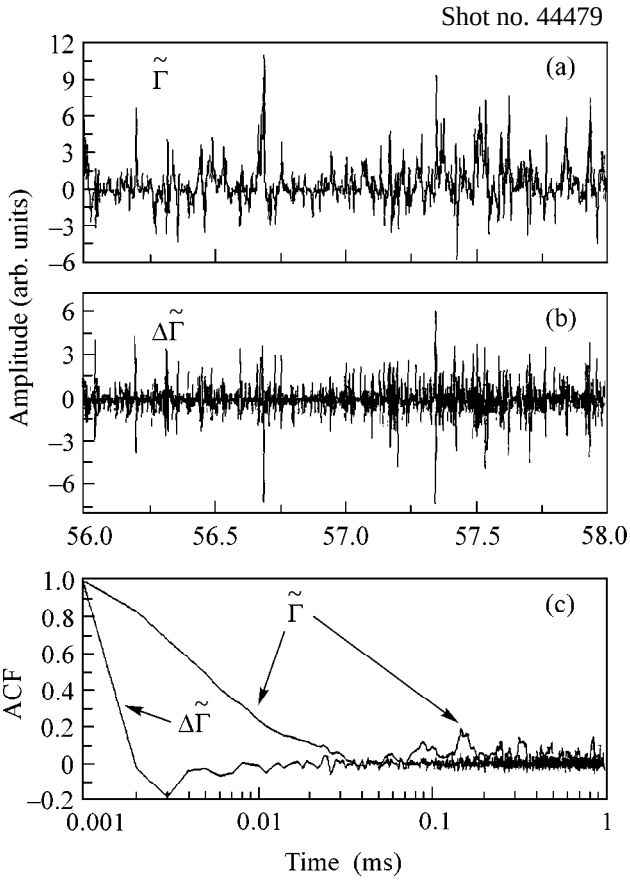

Fig. 1. Time behavior of signals of (a) the fluctuating particle flux $\tilde{\Gamma}$ and (b) its increments $\Delta\tilde{\Gamma}$. (c) Autocorrelation functions $\tilde{\Gamma}$ and $\Delta\tilde{\Gamma}$ for the L-2M device. The signal sampling frequency is 1 MHz.

of fluctuations in the floating potential and the saturation ion current of Langmuir probes for drift oscillations in TAU-1 and MHD oscillations in L-2M. Moreover, the PDF of the increments of the intensity of radiation scattered by density fluctuations in the L-2M plasma core also appears to be symmetric, and the ACF of increments decays with the same constant as that of the increments of the potential and density fluctuations. Apparently, the plasma in both devices is an open system in which the duration of the dynamic equilibrium of macroscopic parameters substantially exceeds the fluctuation times (periods).

As is seen in Fig. 2, the excess coefficients of the PDF for the process $\Delta\tilde{\Gamma}$ are equal to $M_4 \approx 9$ in L-2M and $M_4 \approx 7$ in TAU-1. The latter is of more interest because the corresponding histogram reliably satisfies the model of the Laplacian probability density distribution, whereas both the PDFs of the increments of the fluctuating floating potential and the saturation ion current are Gaussian. The Laplacian distribution is an important special case of the distributions of diffusion

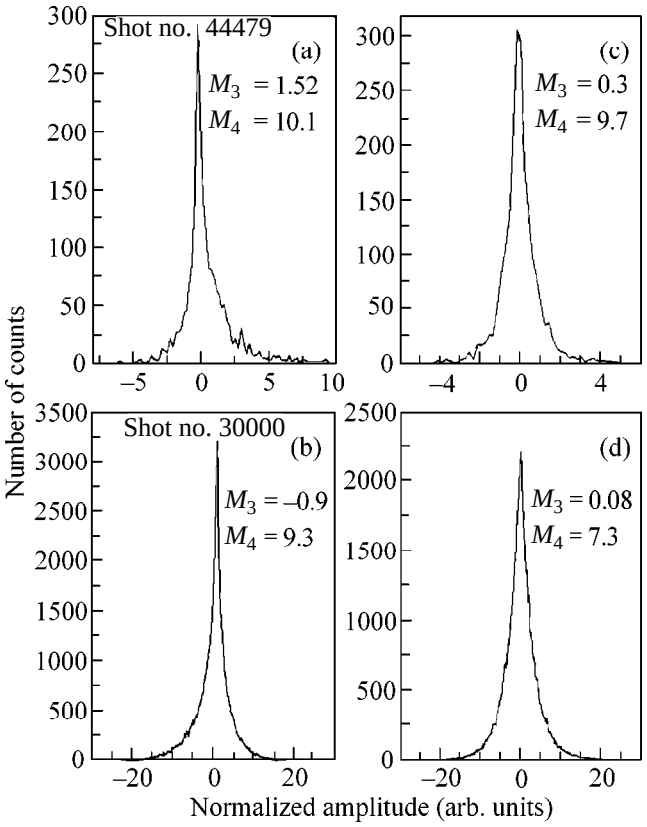

Fig. 2. The probability density functions of (a, b) the local fluctuating particle flux $\tilde{\Gamma}$ and (c, d) its increments $\Delta\tilde{\Gamma}$ in (a, c) L-2M and (b, d) TAU-1.

processes with random time (i.e., doubly stochastic diffusion processes). Such processes result from the passage to the limit in the generalized Cox processes[1] [9]. In this case, the Laplacian probability density distribution (accurate to the scale parameter) can be represented as a scale mixture of Gaussians with an exponential mixing distribution. Thus, if $L(x)$ is a Laplacian distribution function

$$L(x) = \frac{1}{\sqrt{2}}\int_{-\infty}^{\pi} e^{-\sqrt{2}|x|}dx = \left\{\begin{array}{ll} \frac{1}{2}e^{\sqrt{2}x}, & x<0 \\ 1-\frac{1}{2}e^{-\sqrt{2}x}, & x\geq 0 \end{array}\right\}, \quad (1)$$

and $\Phi(x)$ is the standard normal distribution function

$$\Phi(x) = \frac{1}{\sqrt{2\pi}}\int_{-\infty}^{x} e^{-u^2/2}du, \quad (2)$$

then we have

$$L(x) = \int_0^{\infty}\Phi\left(\frac{x}{\sqrt{\sigma}}\right)e^{-\sigma}d\sigma, \quad x \in R \quad (3)$$

(see, e.g., [9]). From here, we can conclude that each increment $\Delta\tilde{\Gamma} = \tilde{\Gamma}_j - \tilde{\Gamma}_{j-1}$ is a result of classical (Brownian) diffusion from the point $\tilde{\Gamma}_{j-1}$ to the point $\tilde{\Gamma}_j$, occurring however with its own diffusion coefficient σ_j, which implies that the fluctuating flux varies with time according to the diffusion law. In this case, as j varies, the coefficient σ_j varies randomly; i.e., the diffusion coefficients σ_j ($j \geq 1$) are random values that obey the exponential distribution [see (1)–(3)].

Another proof of the correctness of describing the fluctuating flux as a diffusion process with random time is that the PDFs of the increments of the drift flux in TAU-1 varies as the time interval between sampling points increases. The Laplacian distribution holds as the interval between the sampling points increases from 1 to 5 μs. As this time interval increases to 100 μs, the PDF transforms into the Gaussian distribution (Fig. 3). Such a transformation corresponds to the asymptotic behavior of the generalized Cox process [9].

Thus, we can conclude that the dynamic characteristics of a fluctuating flux (the growth and damping rates) are random variables obeying the Laplacian law for TAU-1 or a more complicated law (different from the Gaussian distribution) for L-2M. This means that the probability of observing large (more that 3 standard deviations[2]) flux increments distributed by the Laplacian law is many times higher in comparison with the Gaussian law. In other words, the probability of experimentally observing extremely fast variations in the flux increases as compared to the Gaussian law. The PDFs of diffusion processes with random time always have heavier tails and sharper peaks compared to the Gaussian distribution [10]; such a shape of the PDF of fluctuating fluxes is typical of many (not only presented here) devices.

3. Now we consider what physical mechanisms may be responsible for the random character of the dynamic characteristics such as the growth and damping rates of a fluctuating particle flux. Our paper does not pretend to be a comprehensive analysis, since we only briefly examine some physical mechanisms whose role in the formation of the process of random increments is confirmed by the experimental data. The random character of the dynamic parameter of turbulent fluctuations may be a consequence of nonlinear processes limiting the growth of unstable oscillations. Thus, in the case of the beam–plasma or parametric instabilities, such a process may be Langmuir collapse. In the case of drift-dissipative instability, the growth can be limited by stochastic

[1] The Cox process is the doubly stochastic Poisson process defined as $N^{(k)}(t) = N_l(\Lambda_k(t))$, where N_l is a homogeneous Poisson process with unit intensity and Λ_k is a random processes independent of N_l. In [9], the arguments are also presented in favor of using generalized Cox processes as mathematical models for inhomogeneous chaotic physical processes.

[2] In the probability theory, this is known as the "three sigma" rule.

ion heating, which increases plasma diffusion, as was observed in [7].

Another mechanism responsible for the random character of the process of the flux increments $\Delta\tilde{\Gamma}$ may be the generation of nonlinear structures in the turbulent plasma under study both in L-2M (vortices and extended radial MHD structures) and TAU-1 (vortices and solitons) [3, 11] and the interaction among these structures. Previously, we have measured the characteristic turbulence times related to the formation, nonlinear interaction, and damping of such structures. With these times taken into account, the structure of $\Delta\tilde{\Gamma}$ can change significantly.

The incremental analysis gives an opportunity to determine the characteristic time scales on which the nonlinear structures evolve. From this standpoint, it is of great importance that the characteristic dynamic time of the process can be deduced from the ACF of the increments of fluctuations. It is seen from Fig. 1 that for $\Delta\tilde{\Gamma}$, this time is about 1 μs in the edge plasma of L-2M. An analysis of the ACF of the increments of fluctuations in the floating potential and the saturation ion current gives a time of 2 μs. The same value was also obtained for the characteristic time of increments of microwave gyrotron radiation scattered in the core of the plasma column. Since, in the latter case, we measured the scattered signal averaged over a rather large volume near the plasma column axis, we can assume that the dynamic time is the characteristic time of the growth and decay of nonlinear structures.

Similar results were obtained for the characteristic time of the increments of fluctuations in the flux, floating potential, and saturation ion current of Langmuir probes in the case of the drift instability in the TAU-1 plasma.

We draw attention to the fact that the dynamic time is nearly one order of magnitude shorter than the characteristic fluctuation time (the correlation time); i.e., the growth and decay of a nonlinear structure occur by a nonadiabatic law and can be characterized as an abrupt misphasing of the particle motion. From here, we can conclude that the dynamic time, along with the spatial scale length of a nonlinear structure, determines the velocity of fluctuation plasma transport across the magnetic field. Thus, assuming the characteristic scale length of fluctuations in L-2M to be 0.2–1 cm [6] and the dynamic time to be 1–2 μs, we obtain the transport velocity of $1–5 \times 10^5$ cm/s, which is consistent with the probe measurements in the edge plasma [3].

4. The results obtained can be summarized as follows:

(i) A correct statistical analysis of the characteristics of fluctuating particle fluxes based on an equidistant sample of the increments of the fluctuation amplitudes gives an opportunity to determine the characteristic dynamic time of turbulent transport in the L-2M and TAU-1 plasmas. In both cases, this time is one order of magnitude shorter than the characteristic fluctuation time.

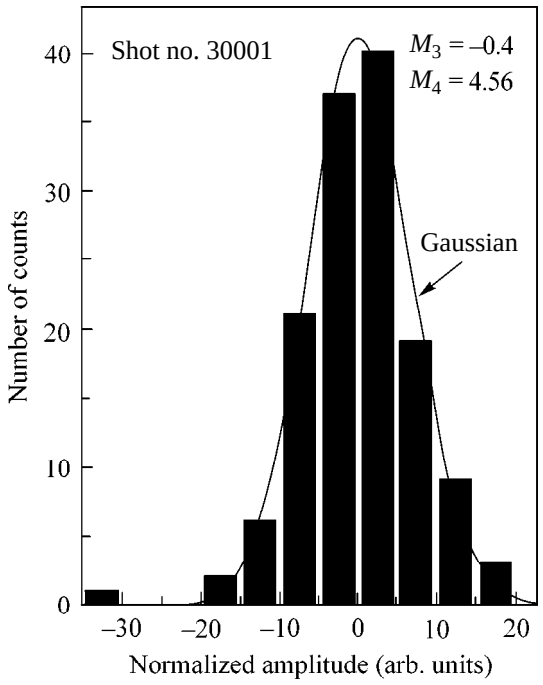

Fig. 3. Histogram of the increments of a local fluctuating particle flux measured at a sampling frequency of 10 kHz in TAU-1.

(ii) It is shown that the increment of the process is a random value and the PDF of the increments of a fluctuating flux is not Gaussian. In the case of drift turbulence in TAU-1, the PDF is described by a Laplace distribution, and, in the case of MHD turbulence, the distribution is more complicated.

(iii) This points to nonlinear processes limiting the growth of unstable oscillations (such as Langmuir collapse, stochastic particle heating, and the formation of nonlinear structures) as possible physical mechanisms responsible for the random character of time variations in the parameters of fluctuation transport in a plasma.

This work was supported in part by the Russian Foundation for Basic Research (project no. 00-02-17507) and the Federal Program “Leading Scientific Schools” (project no. 00-15-96676).

REFERENCES

1. J. W. Connor, P. Burraffi, J. G. Cordey, *et al.*, Plasma Phys. Controlled Fusion **41**, 693 (1999).
2. M. A. Pedrosa, M. A. Ochando, J. A. Jiménez, *et al.*, Plasma Phys. Controlled Fusion **38**, 365 (1996).
3. G. M. Batanov, O. I. Fedyanin, N. K. Kharchev, *et al.*, Plasma Phys. Controlled Fusion **40**, 1241 (1998).

4. B. A. Carreras, B. van Milligen, C. Hidalgo, *et al.*, Phys. Rev. Lett. **83**, 3653 (1999).
5. G. M. Zaslavsky, M. Edelman, H. Weiltzner, *et al.*, Plasma Phys. **7**, 3691 (2000).
6. G. M. Batanov, K. M. Likin, K. A. Sarksyan, and M. G. Shats, Fiz. Plazmy **19**, 1199 (1993) [Plasma Phys. Rep. **7**, 628 (1993)].
7. F. F. Asadullin, G. M. Batanov, L. V. Kolik, *et al.*, Fiz. Plazmy **7**, 414 (1981) [Sov. J. Plasma Phys. **7**, 226 (1981)].
8. G. M. Batanov, K. A. Sarksyan, A. V. Sapozhnikov, *et al.*, in *Proceedings of the IV International Conference on Nonlinear and Turbulent Processes in Physics, Kiev, 1989*, Vol. 1, p. 231.
9. B. V. Gnedenko and V. Yu. Korolev, *Random Summation: Limit Theorems and Applications* (CRC Press, Boca Raton, 1996).
10. I. S. Gradshteyn and I. M. Ryzhik, *Table of Integrals, Series, and Products* (Fizmatgiz, Moscow, 1962; Academic, New York, 1980).
11. A. E. Petrov, K. A. Sarksyan, N. N. Skvortsova, and N. K. Kharchev, Fiz. Plazmy **27**, 58 (2001) [Plasma Phys. Rep. **27**, 56 (2001)].

Translated by N. Larionova

JETP Letters, Vol. 73, No. 3, 2001, pp. 131–134. From Pis'ma v Zhurnal Éksperimental'noĭ i Teoreticheskoĭ Fiziki, Vol. 73, No. 3, 2001, pp. 148–152.

Width of the Zero-Field Superconducting Resistive Transition in the Vicinity of the Localization Threshold[1]

V. F. Gantmakher and M. V. Golubkov

Institute of Solid State Physics, Russian Academy of Sciences, Chernogolovka, Moscow region, 142432 Russia

Received December 28, 2000

Resistive superconducting zero-field transition in amorphous In-O films in the states in the vicinity of the insulator–superconductor transition is analyzed in terms of two characteristic temperatures: the upper T_{c0}, where the finite amplitude of the order parameter is established, and the lower T_c, where the phase ordering takes place. It follows from the magnetoresistance measurements that the resistance in between, $T_c < T < T_{c0}$, cannot be ascribed to the dissipation by thermally dissociated vortex pairs. So, it is not a Kosterlitz–Thouless–Berezinskii transition that occurs at T_c. © *2001 MAIK "Nauka/Interperiodica".*

PACS numbers: 71.30.+h; 74.25.-q; 74.76.Db

The resistive superconducting (*s*) transition in bulk conventional superconductors is very narrow. The reduced width $t \equiv |T - T_{c0}|/T_{c0}$ of the region with strong fluctuations around transition temperature T_{c0} is $t \propto (T_{c0}/\epsilon_F)^4$ in the clean limit and $t \propto (T_{c0}/\epsilon_F)(k_F l)^{-3}$ in the dirty limit, with the product of the Fermi wave vector and mean free path $k_F l > 1$. It is different in 2D, where free magnetic vortices serve as thermal fluctuations. Broad *s* transitions in films were explained by existence of the temperature range where current dissipation is due to these fluctuations [1]. Transition starts at temperature T_{c0}, when Cooper pairs appear in the electronic spectrum. Below T_{c0}, the resistance remains finite because of free vortices. They appear with probability $\mu(T)$ while inbinding vortex–antivortex pairs (magnetic loops). When an external magnetic field is zero, the system of thermal fluctuations contains equal numbers $N_+(T) = N_-(T) = N(T)$ of free vortices of opposite signs. Each vortex lives independently until it annihilates after collision with a vortex of opposite sign. The annihilation probability $\tau^{-1}(T)$, together with probability $\mu(T)$, determines through dynamic equilibrium the concentration $N(T)$:

$$N^2(T) = a(\mu\tau)^{-1}, \quad a = \text{const}. \tag{1}$$

Assuming that there is no pinning, the resistance R is proportional to the total concentration $2N$ of the vortices:

$$R = 2\pi\xi_c^2(2N)R_n, \tag{2}$$

with ξ_c being the effective radius of the vortex core and R_n being the resistance in the normal state. The finite resistance exists until the Kosterlitz–Thouless–Berezinskii (KTB) transition [2] inside the vortex system takes place at some temperature T_c. Below T_c, practically all vortices are bound into loops and $N = 0$. Since loops do not dissipate energy, the resistance vanishes at T_c.

This scheme with two characteristic temperatures was very carefully checked several times with different materials. In particular, Hebard *et al.* [3], in experiments with amorphous InO_x films with $T_{c0} \approx 2.5$ K and $T_c \approx 1.8$ K, have confirmed the transport characteristics predicted by the theory.

In the framework of the BCS theory applied to 2D, both regions controlled by fluctuations, below and above T_{c0}, are narrow differing only by a numerical factor [4]

$$(T_{c0} - T_c)/T_{c0} \approx 3(T - T_{c0})/T_{c0} \approx 3\text{Gi} \ll 1, \tag{3}$$

with Ginzburg parameter Gi being usually small, $\text{Gi} \ll 1$. When the disorder is strong so that the mean free path l reaches its minimum value of k_F^{-1}, the Gi increases and becomes on the order of unity, and the 2D KTB-transition temperature T_c is suppressed compared to T_{c0}, so that the region $T_c < T < T_{c0}$ widens [4]. The vicinity of the superconductor–insulator (*s–i*) transition is just such a region. It is tempting to describe the main part of the broad resistive *s* transitions in terms of vortex-induced dissipation in this case too. However, experiments with granular Pb films [5] demonstrated that the scheme was not universal: the width of the zero-magnetic-field *s* transition for the states in the vicinity of the *s–i* transition was controlled not by thermally activated free vortices.

The width of the fluctuation region t above T_{c0} increases along with $k_F l$ approaching unity: strong disorder makes the fluctuation region wide. This happens not only in 2D [6] but in 3D as well [7, 8], so that specific properties of "short" vortices 2D are not of deci-

[1] This article was submitted by the authors in English.

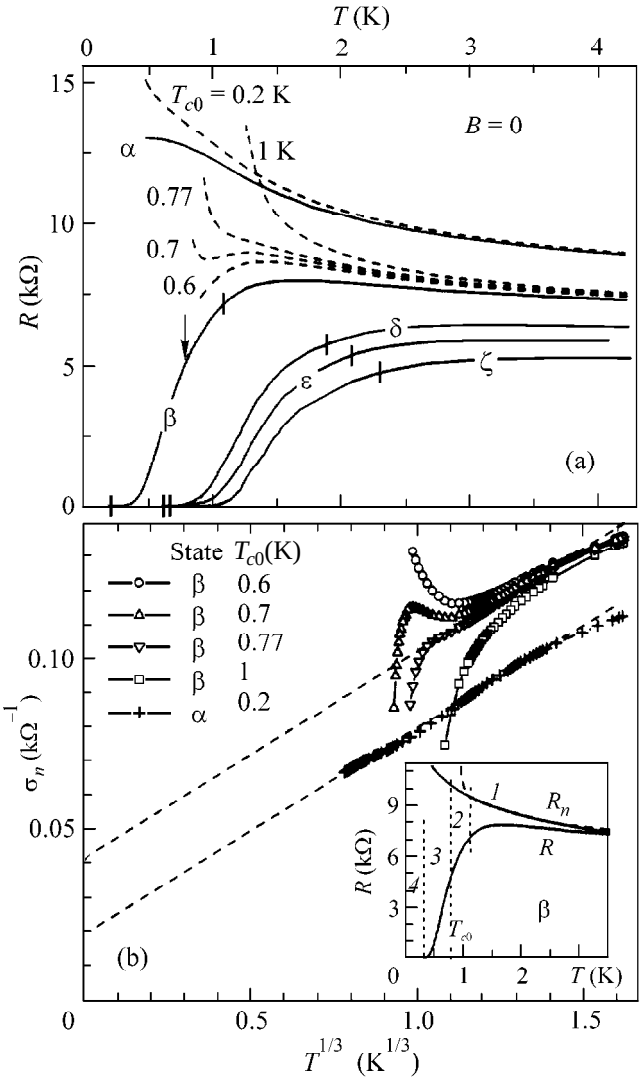

Fig. 1. (a) Zero-field resistive *s* transitions for several states of an amorphous In-O film. Bars frame the transition region ($0.9R_{max}$–$10^{-3}R_{max}$) on the $R(T)$ curves. Dashed curves—one for state α and several, with different values of parameter T_{c0}, for state β—show virtual normal state resistance $R_n^*(T)$ obtained after subtraction of the paraconductivity term calculated in accordance with Eq. (5). The selected value of T_{c0} for state β is shown by the arrow. (b) The dashed curves from panel (a) presented as $\sigma_n^* = (R_n^*)^{-1}$ vs. $T^{1/3}$ (form appropriate for a 3D non-Drude metal in critical region near the metal–insulator transition). Linear extrapolation cuts off the tail from the region of strong fluctuations and transforms σ_n^* into σ_n. Inset: Functions R, R_n, R_n^* (dashed line) for state T_c. About four temperature regions, see text.

sive importance here. Recent approaches for 3D [9] also distinguish between fluctuations of the amplitude of the order parameter and those which destroy long-range phase coherence. In such interpretation, the mean amplitude becomes finite in the vicinity of T_{c0} and the long-range phase coherence establishes itself at $T_c < T_{c0}$. This problem is yet not well understood. Recently Valles *et al.* [10] concluded from tunneling measurements on ultrathin *s* films near the *s*–*i* transition that fluctuations in the amplitude of the superconducting order parameter dominated below T_{c0}.

In [5], the vortex-determined-dissipation scheme was questioned for granular material. Here, we study the same problem for amorphous films, where the disorder is supposed to be on the atomic scale. Our amorphous InO_x films were 200 Å thick. They were certainly 2D from the viewpoint of vortex electrodynamics since the magnetic penetration depth $\lambda \gtrsim 1000$ Å. The 2D character of our films becomes not so obvious when the thickness d is to be compared with some other lengths: various estimates give for the superconducting coherence length ξ_0 a value in the range 100–500 Å, and the magnetic length $l_B = (\hbar c/eB)^{-1/2}$ is 200 Å at $B = 1$ T. The films are 3D in the normal state, since the thickness d is certainly larger then $l \approx k_F^{-1}$.

The properties of the film are determined by the oxygen concentration x [11]. The starting value of x can be changed to some extent by thermal treatment. This affects the carrier concentration and the position of the state in the *s*–*i*-phase diagram [11–13]. We remain in the region where the carrier density n, judging from Hall effect measurements, is in the range (2–4) × 10^{21} cm^{-3} and the parameter $k_F l$ is in the range 0.2–0.3 [11]. Hence, in terms introduced by Emery and Kivelson [9], we deal with a "bad" (non-Drude) metal, where the transport phenomena are not described by Boltzmann theory.

In the experiments, resistive *s* transition $R(T, B)$ is measured. Below, data for several states of one of the films are demonstrated. Results for other films are similar. The aspect ratio of the film is close to one: its resistance R serves, within 10% accuracy, as resistance per square. The measurements were made for six states of the film, labeled α, β, γ, δ, ε, ζ, with *s* properties gradually increasing along this row. Figure 1a shows functions $R(T)$ in zero magnetic field for five of these states. In state α, the *s* transition, if it exists, starts somewhere below $T \lesssim 0.4$ K. For all the others, two conditional temperatures T_{c0} and T_c are marked by bars. They may be considered as the onset and the end of the transition. The upper is positioned at the level $R \approx 0.9R_{max}$, where R_{max} is the value of the maximum in the $R(T)$ curve. The lower is at the level

$$R \approx 10^{-3}R_{max}, \qquad (4)$$

which roughly corresponds to the usual position of the KTB transition [3]. The problem is in the factors that control the shape of the *s* transition in between the marks.

Under the standard approach in conventional superconductors, T_{c0} is determined from experimentally measured $R(T)$ with the help of the expression for the

paraconductivity σ_{fl} due to superconducting fluctuations [14]. In 2D,

$$\sigma = \sigma_n + \sigma_{fl} = \frac{e^2}{\hbar}\left[g + \frac{T_{c0}}{16(T - T_{c0})}\right], \quad \sigma = R^{-1}, \quad \sigma_n = R_n^{-1}. \tag{5}$$

For films far from the localization threshold, the dimensionless sheet conductance is $g \gg 1$ and the correction to R from σ_{fl} soon becomes negligible when T increases above T_{c0}. For our films, g is on the order of unity. Hence, the contribution σ_{fl} really affects the temperature dependence $R(T)$ above T_{c0}.

The term σ_{fl} in Eq. (5) contains T_{c0} as the only parameter which we have to choose. Equation (5) is valid only until the correction is small: $\sigma_{fl} \ll \sigma_n$. Hence, even with right value of parameter T_{c0}, we will get from Eq. (5) function $R_n(T)$ which falsely tends to infinity near T_{c0}. To emphasize this, we will mark these functions by an asterisk, as R_n^*.

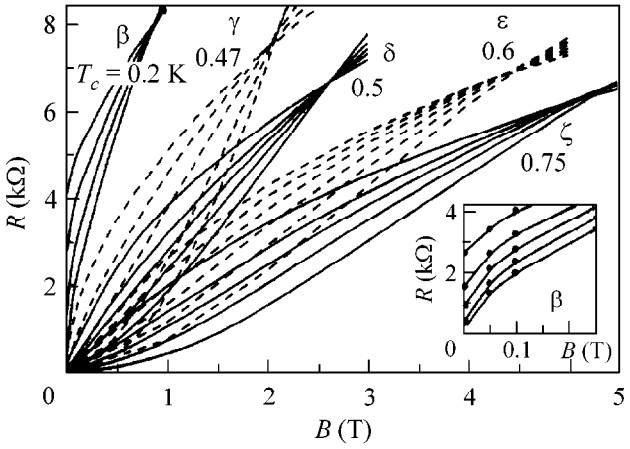

Fig. 2. Magnetoresistance isotherms for a sequence of temperature values for several states of the In-O film. The temperatures in each bunch are downward from 0.85 K with step 0.1 K. About the labeled values of T_c, see text. Inset: denser set of isotherms for state β, down from 0.58 K with step 0.05 K.

Figure 1a presents functions R_n^* for state β, with different values of T_{c0} as a parameter in σ_{fl}. The curve R_n^* obtained with T_{c0} = 1 K has improbably strong temperature dependence below 1.5 K, whereas the curves with T_{c0} = 0.6 and 0.7 K contain maxima. Hence, T_{c0} should be in between.

The specific choice of 0.77 K as T_{c0} is justified by the plot of σ_n vs. $T^{1/3}$ (Fig. 1b). The representation

$$\sigma_n = u + vT^{1/3} \tag{6}$$

is usually used for "bad" 3D metals to distinguish by extrapolation to $T = 0$ metals and insulators (see, for instance, [15]). The chosen value of T_{c0} gives the lowest left-edge value of the temperature interval where data follow Eq. (6). For state β with this T_{c0}, the extrapolated value of $u = \sigma_n(0)$ is $0.15e^2/\hbar$. Note that, according to definition (5), σ_n is 2D conductivity, $\sigma_n \equiv \sigma_n^{(2D)}$, whereas 3D conductivity is $\sigma_n^{(3D)}(0) = \sigma_n^{(2D)}(0)d = (0.15d)e^2/\hbar$.

For state α, the contribution from *s* fluctuations is clearly seen in Fig. 1a as a tendency to decline at low temperatures. The procedures from Fig. 1 applied to this state give T_{c0} = 0.2 K: this is the lowest value of parameter T_{c0} which brings the curve $R_n^*(T)$ without maximum. According to Fig. 1b, the extrapolated value of $\sigma_n(0)$ for state α is twice as small as for state β. One more such step should bring the system to the localization threshold. We know from [11] that this would result in a zero-field *s–i* transition.

Returning to state β, the kink on the curve $\sigma_n(T^{1/3})$ in Fig. 1b reveals the point where fluctuations become so strong that Eq. (5) fails. As is shown in the inset, the temperature axes breaks out into four regions. In the right one, paraconductivity exists. In region *2*, strong superconducting fluctuations prevail. At the opposite end, region *4* is superconducting. Our next task is to study region *3* and to check whether it is the vortex dissipation that controls the resistance in this region, i.e., in the lower part of the transition.

Let us turn to isotherms $R(B)$ in Fig. 2. All the states studied are situated on the *s* side of the phase diagram [12] of the *s–i* transition. Certain critical field values of B_c induce *s–i* transition in these states and bring the sample in the intermediate position between the superconductor and the insulator [16]. The resistance at this field, $R(T, B_c) = R_c$, should not depend on temperature at all [16] or may have only a weak temperature dependence [13]. Hence, the isotherms $R(B, T = \text{const})$ cross in the vicinity of B_c. At low fields, all the isotherms from the vicinity of T_c approach the origin, possibly ending at one of the axes near the origin. Hence, the bunches in Fig. 2 have specific shape of lenses.

Inside each lens, one can more or less confidently select some mean isotherm which separates those with different signs of the second derivative $\partial^2 R/\partial B^2$ inside the interval 0–B_c. Corresponding temperatures of these separating isotherms are written near the bunches. For the left bunches γ and δ, the separating isotherms turn out to be straight lines in the aforementioned interval with the slope $\partial R/\partial B \approx R_c/B_c$. For the states ε and ζ situated deeper in the *s* region, the lenses are slightly deformed and the separating isotherms remain straight only below 2–3 T.

The temperatures of the separating isotherms practically coincide with the values of T_c determined by criterion (4). To some extent, this justifies the choice of the coefficient in criterion (4). On the other hand, we get a

more convenient tool to determine the temperature where the *s* transition becomes complete: by finding the isotherm $R_{T_c}(B)$ which is a linear function going through the origin.

The isotherms with $T > T_c$ cross the ordinate at finite $R(0) \neq 0$. It is clear from the specific shape of the low-field part of the lenses that they have nonzero slope at $B = 0$ (detailed demonstration can be found in the inset in Fig. 2):

$$(\partial R/\partial B)_0 > 0. \quad (7)$$

This linear increase in R exists only with the field perpendicular to the film. The field directed along the film, which does not bring the vortices from outside into the film, results in zero field derivative $(\partial R/\partial B)_0 = 0$, i.e., does not affect dissipation in the linear approximation. This can be seen from the previously published data on In-O films (Fig. 2 in [17]), which compare isotherms for two almost similar states of the film but with different directions of the applied magnetic field.

In the model of thermally excited free vortices, the normal applied field increases the density of vortices of the corresponding sign: $\Delta N_+ \propto B$. But this leads, due to the recombination processes, to the lessening of the density of vortices of opposite sign. When

$$\Delta R \equiv (R(B) - R(0)) \ll R(0), \text{ i.e., } \Delta N_+ \ll N, \quad (8)$$

it follows from dynamic equilibrium equation (1) that $(N + \Delta N_+)(N + \Delta N_-) = N^2$, i.e., that in the linear approximation the density changes cancel each other: $\Delta N_- = -\Delta N_+$. This qualitative inference illustrates the result calculated by Minnhagen [18] long ago: the free vortex density did not change until relation (8) was valid.

Hence, in the framework of the free vortex model, one should expect the resistance change under condition (8) to be $\Delta R = O(B^2)$. Experimental observation that $\Delta R \propto B$ when $\Delta R \ll R(0)$ means that the zero-field resistance R at this temperature is determined not by vortices from thermally dissociated pairs.

Summarizing, we have described the upper part of the resistive *s* transition of a "bad" (non-Drude) metal, amorphous In-O film, by the usual expression [14] for 2D paraconductivity but failed to describe the lower part in terms of an *s* material with thermally excited vortices. Being in line with the idea of two characteristic temperatures, our analysis does not confirm existence of the KTB transition in the vicinity of the lower one. According to Emery and Kivelson [9], separation of onset temperature T_{c0}, where the amplitude of the order parameter is established, and of the phase ordering temperature $T_c < T_{c0}$ happens also in 3D non-Drude metals. Here, the phase-order-breaking thermal fluctuations are certainly not vortices. Our experiment seems to be closer to this model.

We thank V.T. Dolgopolov, A.A. Shashkin, and G.E. Tsydynzhapov for discussions and cooperation in experiments. V.F.G. thanks the Weizmann Institute of Science, Israel, for hospitality and A. Finkelstein, Y. Levinson, M. Schechter, and Y. Oreg for fruitful discussions during his visit, when the final version of this paper was written.

REFERENCES

1. B. I. Galperin and D. R. Nelson, J. Low Temp. Phys. **36**, 599 (1979).
2. V. L. Berezinskii, Zh. Éksp. Teor. Fiz. **59**, 907 (1970) [Sov. Phys. JETP **32**, 493 (1970)]; J. M. Kosterlitz and D. J. Thouless, J. Phys. C **6**, 1181 (1973).
3. A. T. Fiory, A. F. Hebard, and W. I. Glaberson, Phys. Rev. B **28**, 5075 (1983).
4. A. I. Larkin, Ann. Phys. (Leipzig) **8**, 795 (1999).
5. S. R. Khan, E. M. Pedersen, B. Kain, *et al.*, Phys. Rev. B **61**, 5909 (2000).
6. A. Ghosal, M. Randeria, and N. Trivedi, Phys. Rev. Lett. **81**, 3940 (1998).
7. G. Kotliar and A. Kapitulnik, Phys. Rev. B **33**, 3146 (1986).
8. L. N. Bulaevskii, A. A. Varlamov, and M. V. Sadovskii, Fiz. Tverd. Tela (Leningrad) **28**, 1799 (1986) [Sov. Phys. Solid State **28**, 997 (1986)].
9. V. J. Emery and S. A. Kivelson, Phys. Rev. Lett. **74**, 3253 (1995).
10. J. M. Valles, Jr., J. A. Chervenak, S.-Y. Hsu, and T. J. Kouh, cond-mat/0010114.
11. D. Shahar and Z. Ovadyahu, Phys. Rev. B **46**, 10917 (1992).
12. V. F. Gantmakher, M. V. Golubkov, V. T. Dolgopolov, *et al.*, Pis'ma Zh. Éksp. Teor. Fiz. **68**, 337 (1998) [JETP Lett. **68**, 363 (1998)].
13. V. F. Gantmakher, M. V. Golubkov, V. T. Dolgopolov, *et al.*, Pis'ma Zh. Éksp. Teor. Fiz. **71**, 231 (2000) [JETP Lett. **71**, 160 (2000)]; Pis'ma Zh. Éksp. Teor. Fiz. **71**, 693 (2000) [JETP Lett. **71**, 473 (2000)].
14. L. G. Aslamazov and A. I. Larkin, Fiz. Tverd. Tela (Leningrad) **10**, 1104 (1968) [Sov. Phys. Solid State **10**, 875 (1968)].
15. V. F. Gantmakher, V. N. Zverev, V. M. Teplinskii, and O. I. Barkalov, Zh. Éksp. Teor. Fiz. **103**, 1460 (1993) [JETP **76**, 714 (1993)].
16. M. P. A. Fisher, Phys. Rev. Lett. **65**, 923 (1990).
17. V. F. Gantmakher, M. V. Golubkov, V. T. Dolgopolov, *et al.*, Ann. Phys. (Leipzig) **8**, SI-73 (1999).
18. P. Minnhagen, Phys. Rev. B **23**, 5745 (1981); **27**, 2807 (1983).

JETP Letters, Vol. 73, No. 3, 2001, pp. 135–140. Translated from Pis'ma v Zhurnal Éksperimental'noĭ i Teoreticheskoĭ Fiziki, Vol. 73, No. 3, 2001, pp. 153–158.

Stability of the Critical Behavior of Weakly Disordered Systems Against Replica Symmetry Breaking

V. V. Prudnikov*, P. V. Prudnikov, and A. A. Fedorenko

Omsk State University, pr. Mira 55, Omsk, 644077 Russia

** e-mail: prudnikv@univer.omsk.su*

Received November 9, 2000; in final form, December 18, 2000

A field-theoretical approach is used to describe the critical behavior of weakly disordered systems with a *p*-component order parameter. Renormalization group (RG) analysis of the effective replica Hamiltonian of a model with replica-unsymmetrical interaction potential is carried out in a two-loop approximation directly for three-dimensional systems. The Padé–Borel summation technique is used to determine fixed points of the RG equations for the case of a single-step replica symmetry breaking (RSB). Analysis of their stability showed that the type of stable critical behavior of the disordered systems against the RSB effects remains as before. *© 2001 MAIK "Nauka/Interperiodica".*

PACS numbers: 64.60.Ak

In the renormalization-group (RG) description of the critical behavior of disordered systems with quenched disorder, the translational symmetry of the effective Hamiltonian describing fluctuation interactions is reproduced using the replica technique [1–3]. However, the authors of some studies [4–6] have come up with ideas of a possible replica symmetry breaking (RSB) in the systems with quenched disorder. The available physical experiment is capable of neither confirming nor ruling out this hypothesis for the systems with a weak quenched disorder.

In [4, 5], ϵ expansion in a one-loop approximation was used for the RG description of a model disordered system with RSB in the interaction of fourth order with respect to the order parameter fluctuations. It was found that the RSB has a determining effect on the critical behavior of the systems in which the number *p* of order-parameter components is less than four. It has been shown that, for *p* larger than unity but smaller than four, the critical behavior is nonuniversal or, if the model parameters satisfy certain condition as in the Ising systems ($p = 1$), the stable critical state is absent altogether. However, although the conclusions of the cited works are quite intriguing, our previous field-theoretical results obtained for some pure and disordered systems by the method of summation of asymptotic series in a two-loop and higher order approximations have shown [7] that the first-order ϵ-expansion analysis of the stability of various types of critical behavior can be regarded only as a rough estimate, especially for multivertex statistical models [8]. Because of this, the results obtained by Dotsenko *et al.* [4–6] for the RSB effects call for a detailed revision in the context of a more accurate approach.

In this work, the RG description is accomplished for a model of weakly disordered system with RSB in the interaction of fourth order with respect to the order parameter fluctuations. A direct field-theoretical approach, without invoking ϵ expansion, is applied to the three-dimensional systems to solve the RG equations in the two-loop approximation by summation methods, and the analysis of the stability against the RSB effects is performed for various types of critical behavior.

The model Ginzburg–Landau Hamiltonian for a *p*-component spin system with a weak quenched disorder near the critical point reads

$$H = \int d^d x \left\{ \frac{1}{2} \sum_{i=1}^{p} [\nabla \phi_i(x)]^2 + \frac{1}{2}[\tau - \delta\tau(x)] \sum_{i=1}^{p} \phi_i^2(x) + \frac{1}{4} g \sum_{i,j=1}^{p} \phi_i^2(x) \phi_j^2(x) \right\} \quad (1)$$

with the Gaussian-distributed random phase-transition temperature $\delta\tau(x)$, whose dispersion $\langle\langle(\delta\tau(x))^2\rangle\rangle \sim u$ is specified by some positive constant *u* proportional to the concentration of structural defects. The use of the standard replica technique allows straightforward averaging over the temperature fluctuations $\delta\tau(x)$ to reduce the problem of statistical description of a weakly disor-

dered system to the problem of statistical description of a homogeneous system with effective Hamiltonian

$$H_n = \int d^d x \Big\{ \frac{1}{2} \sum_{i=1}^{p} \sum_{a=1}^{n} [\nabla \phi_i^a(x)]^2 + \frac{1}{2} \tau \sum_{i=1}^{p} \sum_{a=1}^{n} [\phi_i^a(x)]^2 + \frac{1}{4} \sum_{i,j=1}^{p} \sum_{a,b=1}^{n} g_{ab} [\phi_i^a(x)]^2 [\phi_j^b(x)]^2 \Big\}, \quad (2)$$

where the index a runs over the replicas (images) of the original homogeneous component in Hamiltonian (1), while the additional vertex u appearing in the interaction matrix $g_{ab} = g\delta_{ab} - u$ specifies the defect-field-induced effective interaction between the fluctuations of the $(n \times p)$-component order parameter. This statistical model is thermodynamically equivalent to the original disordered model in the limit $n \longrightarrow 0$. The subsequent RG procedure of statistical description of the contribution from the long-wavelength order-parameter fluctuations about the ground state with configuration $\phi(x) = 0$ (at $T \geq T_c$), when performed on the scale of correlation length (turning to infinity at the transition temperature T_c), allows one to analyze the possible types of critical behavior of the system and the conditions for their realization and to calculate the critical exponents.

However, it was shown in [4–6] that, due to the fluctuations of the random transition temperature, a macroscopically large number of space domains having $\phi(x) \neq 0$ and separated from the ground state by potential barriers appear in the system at $[\tau - \delta\tau(x)] < 0$. The statistical properties of the systems with a wide range of local energy minima were described in [4–6] using the Parisi RSB formalism. The arguments advanced in [4–6] suggest that, if the replica procedure is applied to the weak disorder, then the statistical description of the contributions from the nonperturbative degrees of freedom associated with the order parameter fluctuations about the configurations of the $\phi(x)$ field in the local energy minima gives rise not to the additional interactions of the $\sum_{a,b} g_{ab} \phi_a^2 \phi_b^2$ type in the effective replica Hamiltonian, where the g_{ab} matrix $g_{ab} = g\delta_{ab} - u$ is no longer replica-symmetric, but to the interactions having the Parisi RSB structure [9]. For instance, according to [4–6, 9], the g_{ab} matrix with the RSB structure is parametrized, in the $n \longrightarrow 0$ limit, in terms of its diagonal elements $\tilde{g}$ and a nondiagonal function $g(x)$ defined on the $0 < x < 1$ interval: $g_{ab} \longrightarrow (\tilde{g}, g(x))$. The corresponding operations on the g_{ab} matrices are given by the following rules:

$$g_{ab}^k \longrightarrow (\tilde{g}^k; g^k(x)),$$

$$(\hat{g}^2)_{ab} = \sum_{c=1}^{n} g_{ac} g_{cb} \longrightarrow (\tilde{c}; c(x)), \quad (3)$$

$$(\hat{g}^3)_{ab} = \sum_{c,d=1}^{n} g_{ac} g_{cd} g_{db} \longrightarrow (\tilde{d}; d(x)),$$

where

$$\tilde{c} = \tilde{g}^2 - \int_0^1 dx g^2(x),$$

$$c(x) = 2\Big[\tilde{g} - \int_0^1 dy g(y)\Big] g(x) - \int_0^x dy [g(x) - g(y)]^2,$$

$$\tilde{d} = \tilde{c}\tilde{g} - \int_0^1 dx c(x) g(x), \quad (4)$$

$$d(x) = \Big[\tilde{g} - \int_0^1 dy g(y)\Big] c(x) + \Big[\tilde{c} - \int_0^1 dy c(y)\Big] g(x) - \int_0^x dy [g(x) - g(y)][c(x) - c(y)].$$

The replica-symmetric situation corresponds to x-independent $g(x) = \text{const}$.

We accomplished the RG description for a model with replica Hamiltonian (2) using the field-theoretical approach in the two-loop approximation directly for the three-dimensional case. The possible types of critical behavior and their stability in the fluctuation region are determined by the RG equations for the coefficients of the g_{ab} matrix. They were determined by the standard method based on the Feynman diagram technique for the vertex parts of irreducible Green's functions and on the renormalization procedure. For example, the resulting two-loop expressions for the two-point $\Gamma^{(2)}$ and the four-point $\Gamma_{ab}^{(4)}$ vertex functions have the form

$$\left.\frac{\partial \Gamma^{(2)}}{\partial k^2}\right|_{k^2=0} = 1 + 4 f g_{aa}^2 + 2 p f \sum_{c=1}^{n} g_{ac} g_{ca}, \quad (5)$$

$$\Gamma_{ab}^{(4)}\big|_{k_i=0} = g_{ab} - p \sum_{c=1}^{n} g_{ac} g_{cb} - 4 g_{aa} g_{ab} - 4 g_{ab}^2 + (8 + 16h) g_{ab}^3 + (24 + 8h) g_{aa}^2 g_{ab}$$

$$+ 48hg_{aa}g_{ab}^2 + 4g_{aa}g_{bb}g_{ab} + 8ph\sum_{c=1}^{n} g_{ac}g_{cb}^2$$
$$+ 8phg_{ab}\sum_{c=1}^{n} g_{ac}g_{cb} + 4phg_{ab}\sum_{c=1}^{n} g_{ac}^2$$
$$+ 2p\sum_{c=1}^{n} g_{ac}g_{cc}g_{cb} + 4pg_{aa}\sum_{c=1}^{n} g_{ac}g_{cb}$$
$$+ p^2\sum_{c,d=1}^{n} g_{ac}g_{cd}g_{db}, \quad (6)$$

where the following notation is introduced:

$$f(d) = -\frac{1}{J^2}\frac{\partial}{\partial k^2} \times \int \frac{d^d k_1 d^d k_2}{(k_1^2+1)(k_2^2+1)((k_1+k_2+k)^2+1)}\bigg|_{k^2=0}, \quad (7)$$

$$h(d) = \frac{1}{J^2}\int \frac{d^d k_1 d^d k_2}{(k_1^2+1)^2(k_2^2+1)((k_1+k_2)^2+1)}, \quad (8)$$

$$J = \int d^d k/(k^2+1)^2, \quad f(d=3) = \frac{2}{27}, \quad h(d=3) = \frac{2}{3}, \quad (9)$$

and g_{ab} is redefined as $g_{ab} \longrightarrow g_{ab}/J$. However, the subsequent renormalization of the vertex functions, as well as the determination of the β functions specifying RG transformations for the interaction constants, is hampered because of the complicated character of Eqs. (3) and (4) for the operations on the g_{ab} matrices. The step structure, revealed in [4–6] for the $g(x)$ function, allows the realization of the renormalization procedure. In this work, we restrict ourselves to the single-step $g(x)$ functions of the form

$$g(x) = \begin{cases} g_0, & 0 \le x < x_0 \\ g_1, & x_0 < x \le 1, \end{cases} \quad (10)$$

where the step coordinate $0 \le x_0 \le 1$ is an arbitrary scaling-invariant parameter and remains the same as in the bare function $g_0(x)$. As a result, the RG transformations of the replica Hamiltonian with RSB are specified by three parameters $\tilde{g}$, g_0, and g_1. The β functions obtained for them in the two-loop approximation read

$$\beta_1 = -\tilde{g} + (p+8)\tilde{g}^2 - px_0 g_0^2 - p(1-x_0)g_1^2 + \frac{4}{27}(41p+190)\tilde{g}^3 + \frac{92}{27}px_0\tilde{g}g_0^2 + \frac{92}{27}p(1-x_0)\tilde{g}g_1^2 + \frac{8}{3}px_0 g_0^3 + \frac{8}{3}p(1-x_0)g_1^3,$$

$$\beta_2 = -g_0 + (4-2px_0)g_0^2 + (4+2p)\tilde{g}g_0 - 2p(1-x_0)g_0 g_1 + \frac{16}{3}\left(\frac{77}{36}px_0 - 1\right)g_0^3 - \frac{92}{27}(p+2)\tilde{g}^2 g_0 + \frac{8}{3}(2px_0 - 5p - 6)\tilde{g}g_0^2 + \frac{40}{3}p(1-x_0)g_0^2 g_1 - \frac{52}{27}p(1-x_0)g_0 g_1^2 + \frac{16}{3}p(1-x_0)\tilde{g}g_0 g_1,$$

$$\beta_3 = -g_1 + (px_0 - 2p + 4)g_1^2 - px_0 g_0^2 + (4+2p)\tilde{g}g_1 - \left(\frac{92}{27}px_0 - \frac{308}{27}p + \frac{16}{3}\right)g_1^3 + \frac{8}{3}px_0 g_0^3 - \frac{92}{27}(p+2)\tilde{g}^2 g_1 + \frac{8}{3}px_0\tilde{g}g_0^2 - \left(\frac{8}{3}px_0 + 8p + 16\right)\tilde{g}g_1^2 + \frac{20}{27}px_0 g_0^2 g_1. \quad (11)$$

It is known that the perturbation series are asymptotic, while the vertices corresponding to the interaction of order parameter fluctuations in the fluctuation region $\tau \longrightarrow 0$ are too large for Eqs. (11) to be used directly. For this reason, to extract the desired physical information from the derived expressions, we applied the generalized Padé–Borel method, which is used for the summation of asymptotic series. The direct and inverse Borel transformations extended to the three-parameter case are given by

$$f(\tilde{g}, g_0, g_1) = \sum_{i,j,k} c_{ijk}\tilde{g}^i g_0^j g_1^k = \int_0^\infty e^{-t}F(\tilde{g}t, g_0 t, g_1 t)dt, \quad (12)$$

$$F(\tilde{g}, g_0, g_1) = \sum_{i,j,k} \frac{c_{ijk}}{(i+j+k)!}\tilde{g}^i g_0^j g_1^k.$$

For the analytic continuation of the Borel transform, the expansion in powers of an auxiliary variable θ is introduced,

$$\tilde{F}(\tilde{g}, g_0, g_1, \theta) = \sum_{k=0}^{\infty}\theta^k\sum_{i=0}^{k}\sum_{j=0}^{k-i}\frac{c_{i,j,k-i-j}}{k!}\tilde{g}^i g_0^j g_1^{k-i-j}, \quad (13)$$

to which the Padé approximation [L/M] is applied at the point θ = 1. In the two-loop calculation of β functions, we used the [2/1] approximant. The type of criti-

cal behavior is determined by the presence of a stable fixed point satisfying the system of equations

$$\beta_k(\tilde{g}^*, g_0^*, g_1^*) = 0 \quad (k = 1, 2, 3). \tag{14}$$

The solution of the system of Eqs. (14) for the $p = 1, 2,$ and 3 numbers of order-parameter components gave three types of nontrivial fixed points in the physically reasonable range of parameters $\tilde{g}^* > 0$, $g_0^* \le 0$, and $g_1^* \le 0$ (Tables 1–3). For instance, a fixed point with $\tilde{g}^* \neq 0$ and $g_0^* = g_1^* = 0$ corresponds to the critical behavior of a pure system; a point with $\tilde{g}^* \neq 0$ and $g_0^* = g_1^* \neq 0$ corresponds to the critical behavior of a replica-symmetric disordered system; and a point with $\tilde{g}^* \neq 0$, $g_0^* = 0$, and $g_1^* \neq 0$ corresponds to the critical behavior of a disordered system with RSB. The parameters $\tilde{g}^*$ and g_1^* at a fixed point with RSB depend on the step coordinate x_0, so that the corresponding $\tilde{g}^*$ and g_1^* values are given in Tables 1–3 for $0 \le x_0 \le 1$ with a step of $\Delta x_0 = 0.1$.

The possibility of obtaining critical behavior of a particular type is determined for each p by the stability of the corresponding fixed point. The stability requirement on the fixed point amounts to the condition that the eigenvalues λ_i of the matrix

$$B_{i,j} = \frac{\partial \beta_i(\tilde{g}^*, g_0^*, g_1^*)}{\partial g_j} \tag{15}$$

lie in the right complex half-plane. An analysis of the λ_i values for fixed points of each type (Tables 1–3) allows the following conclusions to be drawn: for the Ising model ($p = 1$), the stable replica-symmetric fixed point corresponds to a disordered system; with the XY model ($p = 2$), we are inclined to believe that, in spite of the fact that the positive λ_i are indicative of a weakly stable replica-symmetric fixed point, the stable fixed point in the higher order approximation will correspond to the critical behavior of a pure system, as in the case of disordered systems not including the RSB effects [10]; for the isotropic Heisenberg model ($p = 3$), the stable fixed point corresponds to a pure system.

It is noteworthy that the obtained vertex values $\tilde{g}^*$ and g_0^* and the eigenvalues λ_i of the stability matrix at the replica-symmetric fixed points are in good agreement with the results of [10], where the disordered three-dimensional spin systems were studied in the two-loop approximation using summation methods. When comparing both results, account should be taken of the fact that the v_1 and v_2 vertices introduced in [10] are related to the $\tilde{g}$ and g_0 vertices as $v_1 = (p + 8)(\tilde{g} + 9g_0)$ and $v_2 = 8g_0$. Due to this transformation and to the influence of the third vertex g_1, the λ_i eigenvalues of the stability matrix undergo some changes at the corresponding fixed points, although the overall relative character of their stability is retained. We calculated some of the critical exponents for a three-dimensional disordered Ising model and pure models with $p = 1, 2,$ and 3. The resulting Padé–Borel resummed values (except for the critical exponent η, for which the two-loop approximation is the lowest order approximation of the theory) are given in Table 4, where they are also compared with the corresponding critical exponents taken from [11, 12], in which the calculations were carried out for the three-dimensional models in the as yet supreme six-loop approximation. It follows from Table 4 that the two-loop calculations performed directly for the three-dimensional systems by using the summation method are reliable enough for the results obtained for the RSB effects to be trustworthy. The presently avail-

Table 1. Fixed points and eigenvalues for $p = 1$

Type	x_0	$\tilde{g}^*$	g_0^*	g_1^*	λ_1	λ_2	λ_3
1		0.1774103	0	0	0.65355	−0.16924	−0.16924
2		0.1843726	−0.0812240	−0.0812240	$0.525 \pm 0.089i$		0.211
3	0.0	0.1843726	0	−0.0812240	$0.525319 \pm 0.089273i$		−0.039167
	0.1	0.1839722	0	−0.0829404	$0.535185 \pm 0.098291i$		−0.049185
	0.2	0.1835134	0	−0.0846432	$0.547065 \pm 0.106665i$		−0.059851
	0.3	0.1829917	0	−0.0863186	$0.560666 \pm 0.113305i$		−0.071187
	0.4	0.1824035	0	−0.0879503	$0.576473 \pm 0.118038i$		−0.083210
	0.5	0.1817458	0	−0.0895200	$0.595060 \pm 0.120271i$		−0.095927
	0.6	0.1810165	0	−0.0910067	$0.617241 \pm 0.118872i$		−0.109334
	0.7	0.1802154	0	−0.0923872	$0.643936 \pm 0.111389i$		−0.123415
	0.8	0.1793442	0	−0.0936384	$0.675972 \pm 0.092079i$		−0.138133
	0.9	0.1784070	0	−0.0947426	$0.713456 \pm 0.035266i$		−0.153431
	1.0	0.1774103	0	−0.0956920	0.857325	0.65355	−0.169237

Table 2. Fixed points and eigenvalues for $p = 2$

Type	x_0	$\tilde{g}^*$	g_0^*	g_1^*	λ_1	λ_2	λ_3
1		0.1558303	0	0	0.667315	−0.001672	−0.001672
2		0.1558310	−0.0005837	−0.0005837	0.667312	0.001682	0.000004
3	0.0	0.1558310	0	−0.0005837	0.667313	0.001683	−0.000001
	0.1	0.1558310	0	−0.0006143	0.667313	0.001684	−0.000088
	0.2	0.1558310	0	−0.0006483	0.667313	0.001685	−0.000186
	0.3	0.1558310	0	−0.0006863	0.667313	0.001686	−0.000296
	0.4	0.1558310	0	−0.0007291	0.667313	0.001687	−0.000419
	0.5	0.1558310	0	−0.0007775	0.667313	0.001687	−0.000559
	0.6	0.1558309	0	−0.0008327	0.667313	0.001688	−0.000717
	0.7	0.1558308	0	−0.0008964	0.667314	0.001690	−0.000901
	0.8	0.1558307	0	−0.0009707	0.667314	0.001692	−0.001116
	0.9	0.1558306	0	−0.0010583	0.667315	0.001694	−0.001369
	1.0	0.1558303	0	−0.0011633	0.667316	0.001696	−0.001672

Table 3. Fixed points and eigenvalues for $p = 3$

Type	x_0	$\tilde{g}^*$	g_0^*	g_1^*	λ_1	λ_2	λ_3
1		0.1382700	0	0	0.681378	0.131537	0.131537
2		0.2744341	−0.2678523	−0.2678523	1.092061	−14.99922	−18.30806
3	0.0	0.2744341	0	−0.2678523	1.092061	−14.99922	1.745304
	0.1	0.2578105	0	−0.2562879	1.050832	−13.86676	1.564010
	0.2	0.2417139	0	−0.2447617	1.007715	−12.80855	1.384946
	0.3	0.2261734	0	−0.2332726	0.963140	−11.82213	1.208653
	0.4	0.2112310	0	−0.2218288	0.917697	−10.90542	1.035821
	0.5	0.1969437	0	−0.2104508	0.867311	−10.05682	0.872158
	0.6	0.1833842	0	−0.1991760	0.704176	−9.275142	0.827493
	0.7	0.1706399	0	−0.1880615	0.547650	−8.559373	0.784850
	0.8	0.1588089	0	−0.1771867	0.399112	−7.908429	0.745485
	0.9	0.1479902	0	−0.1666512	0.259975	−7.320732	0.710644
	1.0	0.1382700	0	−0.1565674	0.131537	−6.793766	0.681378

able experimental values of critical exponents obtained for Ising-like disordered systems are presented rather comprehensively in [12, 13], where the calculated and experimental critical exponents are shown to be in good agreement within the corresponding accuracies. Note also that the results obtained by the ε expansion for the multivertex statistical models without regard for the order of approximation are not reliable. This was demonstrated both by our analysis of the effective three-vertex model and by the models used in other studies [7, 8, 13]. Such a situation is explained by the competition between the different types of fixed points in the parametric space of multivertex models. As a rule, this competition prevents completion of the $\varepsilon \longrightarrow 1$ transition without intersection of marginal dimensionalities $3 < d_c < 4$ separating the stability domains of different fixed points. In contrast to the marginal number p_c of order-parameter components (the XY model with p_c close to 2), a search for d_c in the field-theoretical approach is hampered by the complexity of evaluating diagrammatic integrals for arbitrary dimensionality d.

In summary, the two-loop renormalization-group studies of the three-dimensional weakly disordered systems have shown that their critical behavior is stable against the effects of replica symmetry breakdown. For the systems with a one-component order parameter, the critical behavior is determined by the structural disorder with a replica-symmetric fixed point. Weak disorder has no effect on the critical behavior of the multicomponent systems, although higher order calculations are

Table 4. Critical exponents at replica-symmetric (RS) fixed points (FP) for three-dimensional models

Model	FP	η	ν	γ	β	α
Ising	RS1	0.0280	0.6311	1.2445	0.3244	0.1068
	[11]	0.031(4)	0.630(2)	1.241(2)	0.325(2)	0.110(5)
	RS2	0.0283	0.6718	1.3294	−0.0154	0.3454
	[12]	0.030(3)	0.678(10)	1.330(17)	−0.034(30)	0.349(5)
XY	RS1	0.0288	0.6673	1.3187	0.3427	−0.0019
	[11]	0.034(3)	0.669(1)	1.316(1)	0.346(1)	−0.007(6)
Heisenberg	RS1	0.0283	0.6972	1.3787	0.3585	−0.0916
	[11]	0.034(3)	0.705(1)	1.387(1)	0.364(1)	−0.115(9)

required to prove this statement for the systems with $p = 2$. In our opinion, the revelation of the possible manifestations of the replica symmetry breakdown effects in the critical behavior of strongly disordered systems can be accomplished by nonperturbative methods through computer simulation of the order parameter fluctuation distribution function and the random transition temperature fluctuation spectrum [14].

This work was supported by the Russian Foundation for Basic Research, project no. 00-02-16455.

REFERENCES

1. S. F. Edwards and P. W. Anderson, J. Phys. F **5**, 965 (1975).
2. J. Emery, Phys. Rev. B **11**, 239 (1975).
3. G. Grinstein and A. Luther, Phys. Rev. B **13**, 1329 (1976).
4. Vik. S. Dotsenko, A. B. Harris, D. Sherrington, and R. B. Stinchcombe, J. Phys. A **28**, 3093 (1995).
5. Vik. S. Dotsenko and D. E. Feldman, J. Phys. A **28**, 5183 (1995).
6. Vik. S. Dotsenko, Usp. Fiz. Nauk **165**, 481 (1995) [Phys. Usp. **38**, 457 (1995)].
7. V. V. Prudnikov, A. V. Ivanov, and A. A. Fedorenko, Pis'ma Zh. Éksp. Teor. Fiz. **66**, 793 (1997) [JETP Lett. **66**, 835 (1997)]; V. V. Prudnikov, S. V. Belim, A. V. Ivanov, *et al.*, Zh. Éksp. Teor. Fiz. **114**, 972 (1998) [JETP **87**, 527 (1998)]; V. V. Prudnikov, P. V. Prudnikov, and A. A. Fedorenko, Zh. Éksp. Teor. Fiz. **116**, 611 (1999) [JETP **89**, 325 (1999)]; V. V. Prudnikov, P. V. Prudnikov, and A. A. Fedorenko, Phys. Rev. B **62**, 8777 (2000).
8. K. B. Varnashev and A. I. Sokolov, Fiz. Tverd. Tela (St. Petersburg) **38**, 3665 (1996) [Phys. Solid State **38**, 1996 (1996)]; A. I. Sokolov, K. B. Varnashev, and A. I. Mudrov, Int. J. Mod. Phys. B **12**, 1365 (1998); A. I. Sokolov and K. B. Varnashev, Phys. Rev. B **59**, 8363 (1999).
9. M. Mezard and G. Parisi, J. Phys. I **1**, 809 (1991); M. Mezard, G. Parisi, and M. Virasoro, *Spin-Glass Theory and Beyond* (World Scientific, Singapore, 1987).
10. G. Jug, Phys. Rev. B **27**, 609 (1983).
11. J. C. Le Guillou and J. Zinn-Justin, Phys. Rev. B **21**, 3976 (1980).
12. A. Pelissetto and E. Vicari, cond-mat/0002402.
13. R. Folk, Yu. Holovatch, and T. Yavors'kii, cond-mat/9909121.
14. M. M. Tsypin, Phys. Rev. B **55**, 8911 (1997).

Translated by V. Sakun

JETP Letters, Vol. 73, No. 3, 2001, pp. 141–144. From Pis'ma v Zhurnal Éksperimental'noĭ i Teoreticheskoĭ Fiziki, Vol. 73, No. 3, 2001, pp. 159–162.

Superconducting Energy Gap in $Bi_2Sr_2Ca_2Cu_3O_{10+\delta}$ (Bi2223) Single Crystals[1]

S. I. Vedeneev and V. A. Stepanov

Lebedev Institute of Physics, Russian Academy of Sciences, Leninskiĭ pr. 53, Moscow, 117924 Russia

Received December 28, 2000

Current–voltage characteristics of *S–I–S* tunnel break junctions fabricated from pure undoped Bi2223 single crystals (T_c = 110 K) were measured. High quality of the crystals enabled production of good tunnel junctions with a low or almost zero leakage current and well developed gap structure in the tunneling spectra. The peak-to-peak energy gap values $2\Delta_{p-p}$ in different crystals and the tunnel junctions ranged from 80 to 105 meV. The tunneling conductance in the superconducting state was normalized to that in the normal state and compared to a smeared BCS density of states. A simple fit of the data gave the average value of Δ = 38.5 meV and reduced gap $2\Delta/kT_c \simeq 8$, consistent with a very strong coupling mechanism. © *2001 MAIK "Nauka/Interperiodica".*

PACS numbers: 74.50.+r; 74.72.Hs

An investigation of the tunneling conductance is very important for the understanding of the mechanism of superconductivity in high-T_c superconductors. Tunneling spectroscopy was very successful in studying the superconducting state in conventional superconductors. However, a rich variety of peculiarities observed in the tunneling spectra of high-T_c superconductors hampers a unique analysis of the experimental results. It seems likely that most of these unusual tunneling data can be attributed to the inferior quality of the tunneling junctions studied. The shape of the current–voltage (*I–V*) characteristics are far from the ideal that, for the conventional superconductors and the tunneling junctions, as a rule, do not meet the well-known requirements for the junction selection. In particular, there are scarcely any *I–V* characteristics satisfying Ohm's law at voltages above the superconducting energy gap. In addition, single crystals of layered high-T_c superconductors often contain a large number of very thin interlayers of the other phases. At present, most of the reproducible results have been obtained for bilayered cuprate $Bi_2Sr_2CaCu_2O_{8+\delta}$ (Bi2212) only. Up to now, there has been no definiteness in the dependence of the superconducting energy gap 2Δ and $2\Delta/kT_c$ ratio on the doping level [1, 2]. In this connection, it is important to measure the gap value in the higher-T_c phase Bi2223 since the problem of oxygen deficiency is less dramatic in the Bi compounds. For lack of single crystals, the data on 2Δ in Bi2223 have been very limited. The low temperature gap values were only measured on ceramic samples with a mixture of Bi2212 and Bi2223 phases [3–5]. The exception is the STM experiments [6] where *c*-axis-oriented Bi2223 polycrystals were used.

In operation of our previous tunneling studies of the high-T_c and low-T_c Bi-family superconductors [7, 8], we present here first results on the tunneling measurements in several pure undoped Bi2223 single crystals by using a break-junction technique. The high quality of Bi2223 samples enables us to fabricate good tunnel junctions with a low or almost zero leakage current and well-developed gap structure in the tunneling spectra.

$Bi_{2.11}Sr_{2.02}Ca_{1.75}Cu_{2.8}O_{10+\delta}$ single crystals with T_c(midpoint) = 110 K and ΔT_c = 2.5 K (10–90% transition points) were obtained by free growth in gas cavities formed in KCl solution melt [9]. The crystals had a plateletlike rectangular shape and mirror surfaces. The sizes of the crystals were around $1 \times 1 \times 0.003$ mm. The quality of the crystals was verified by the measurements of the dc resistance, ac susceptibility, X-ray diffraction, and scanning electron microscopy. It should be noted that the onset temperature of superconducting transitions and the transition widths for dc resistance and ac susceptibility were very close. Composition of the crystals was studied at the Laboratory of Solid State Physics, University of Groningen, The Netherlands. The X-ray studies showed that the crystals studied here contained less than 3% of the Bi2212 phase, as indicated by a slightly increased width of certain reflections in the diffraction patterns [9]. The unit cell parameters were equal to a = 5.38 Å and c = 36.95 Å. Details of break-junction preparation are described by us elsewhere [7].

In Fig. 1a, we plotted the *I–V* characteristics of the tunnel break junctions at T = 4.2 K fabricated from

[1] This article was submitted by the authors in English.

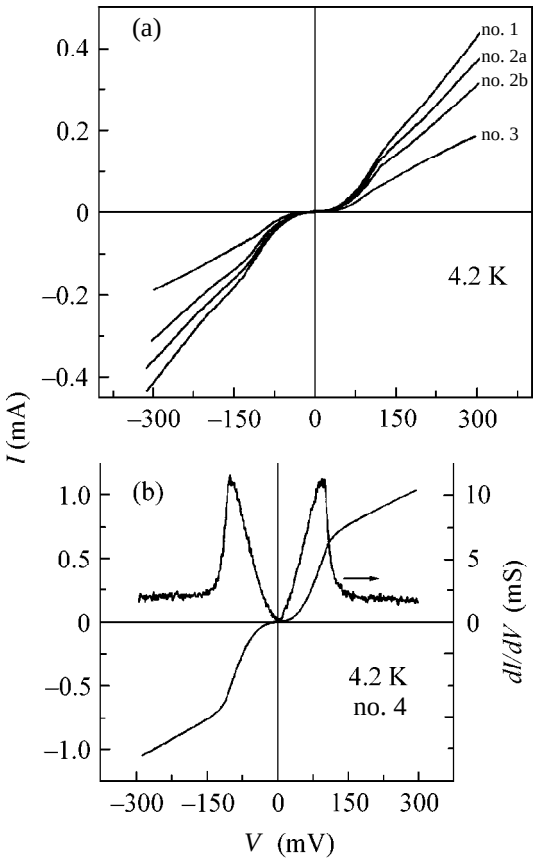

Fig. 1. (a) *I–V* characteristics of the tunnel break junctions at 4.2 K fabricated from three Bi2223 single crystals. (b) The representative *I–V* and *dI*/*dV* vs. *V* characteristics for low-resistance tunnel junction. The inferior quality of the tunneling barrier leads to considerable distortion of the curves.

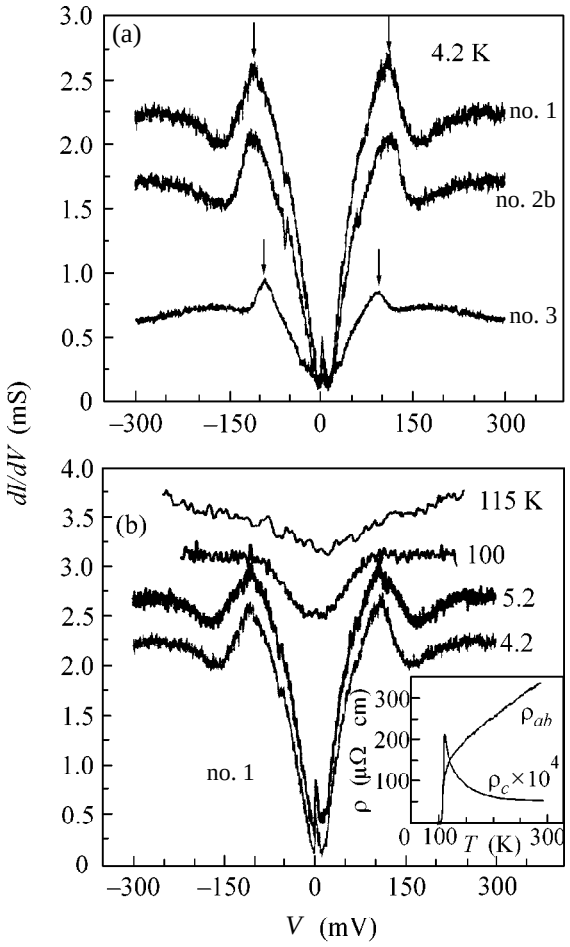

Fig. 2. (a) The tunneling conductance data *dI*/*dV* vs. *V* measured on the three crystals at 4.2 K. The arrows marked the peak positions to determine the superconducting energy gap value $2\Delta_{p-p}$. (b) The tunneling conductance *dI*/*dV* vs. *V* at selected temperatures for one of the single crystals (no. 1). The curves have been shifted vertically with respect to the 4.2 K curve, for clarity. The inset shows the temperature dependences of in-plane and out-of-plane resistivities measured on the same crystals.

three Bi2223 single crystals. The curves are reproducible and reveal the characteristic features for a superconducting tunnel junction with a flat region around zero bias voltage and a well-defined sharp increase in the tunnel current around $V = \pm(90–100)$ mV connected with a superconducting energy gap. At $|V| > |100|$ mV, the *I–V* characteristics are linear and located in line with the zeroth point, as it must be for good tunnel junctions.

It is known that the break-junction technique allows one to control the junction resistance and change the shape of the *I–V* characteristics. Figure 1b shows the representative *I–V* curve along with the tunneling conductance data *dI*/*dV* vs. *V* for a low-resistance tunnel junction, which are of frequent occurrence in experiments with high-T_c superconductors. The inferior quality of the tunneling barrier leads to considerable distortion of the *I–V* and *dI*/*dV*(*V*) curves. For junctions of this type, even Ohm's law does not hold. Although the gap feature in this curve is more pronounced than in the classical curves, it is strongly changed and these curves are unusable for a tunneling density of states determination.

Figure 2a shows the tunneling conductance data *dI*/*dV*(*V*) measured on three crystals at $T = 4.2$ K. The shapes of the *dI*/*dV*(*V*) curves are very similar to those for the tunneling conductance of Bi2212 [7] which were compatible with a smeared BCS density of states. For the *S–I–S* junctions studied here, the peak-to-peak distance between the two main maxima (marked by arrows) on the *dI*/*dV*(*V*) curves corresponds to $4\Delta_{p-p}$.

The values of the energy gap $2\Delta_{p-p}$ in different crystals and tunnel junctions ranged from 80 to 105 meV. It should be noted that the data in Fig. 2a correspond to tunnel junctions with the minimal and maximal values of $2\Delta_{p-p}$. The sharp peak in the low-temperature conductances at zero-bias voltage as in the case of Bi2212 results from the Josephson current. It has been previ-

ously shown by us [7] that this peak can be suppressed by a magnetic field.

To determine the relation between Δ and T_c, we measured the tunneling conductance $dI/dV(V)$ at selected temperatures on one of single crystals (no. 1). The results are shown in Fig. 2b. For clarity, the curves have been shifted relative to the lower curve. In the inset, we show the temperature dependences of the in-plane and out-of-plane resistivities measured on the same crystal. One can see that the gap structure broadens and diminishes at increasing temperature. Since T_c for given sample was equal 110 K, and the gap structure vanished completely at a temperature close to T_c, we can infer that the observed energy gap is surely the superconducting state gap of Bi2223.

In order to find out a relation between Δ and T_c, we normalized the smoothed conductance $dI/dV(V)_S$ of the junction in the superconducting state at 5.2 K by the smoothed conductance $dI/dV(V)_N$ in the normal state at 115 K, which are displayed in Fig. 3a. Thereafter, we made a least-squares fit of the expression

$$dI/dV(V)_S/dI/dV(V)_N = \frac{d}{deV}\int_0^{eV} N(E)N(E-eV)dE \qquad (1)$$

to the normalized tunneling conductance, where $N(E) = \mathrm{Re}[(E - i\Gamma)/\sqrt{(E - i\Gamma)^2 - \Delta^2}\,]$ is a smeared BCS density of states. Here, Γ is a measure of the quasiparticle scattering rate [10]. The modified BCS curve (dashed line in Fig. 3b) indicates that a reasonable fit of the gap region of the T = 5.2 K data is achieved with Δ = 44 meV and Γ = 21.5 meV, except for a small region near zero, where the Josephson effect influences the measurements and the strong dips at ±170 mV, that has been observed in many other tunneling studies of Bi2212 single crystals. Recent tunneling experiments by DeWilde *et al.* [2] suggested that this dip feature in the conductance is due to a strong-coupling effect in *d*-wave superconductors and it arises from a frequency dependence of an electron–electron pairing interaction. The fit to the data with minimal value of Δ for crystal no. 3 gave values Δ = 33 meV and Γ = 15 meV. The obtained average value of Δ = 38.5 meV agrees closely with the earlier measurements of the energy gap on *c*-axis-oriented Bi2223 polycrystals [6], where Δ = 38 meV was obtained. The values of the ratio $2\Delta/kT_c$ for our two crystal nos. 1 and 3 are 9.2 and 7, respectively. The average value of the reduced gap $2\Delta/kT_c \simeq 8$ corresponds to a very strong coupling mechanism.

In a recent tunneling study [1] of Bi2212 single crystals with various oxygen concentrations, a strong dependence of the energy gap 2Δ on oxygen doping was observed. By measuring the normal-state Hall coefficient in our crystals, we have found that the concentration of the carriers n in samples is near 4×10^{21} cm^{-3}. Once the values of T_c and n in our single crystals are closely matched by those in the optimaly doped (Bi, Pb)2223 ceramic samples [11], one can believe that the magnitudes of 2Δ and $2\Delta/kT_c$ found here are related to the optimaly doped crystals.

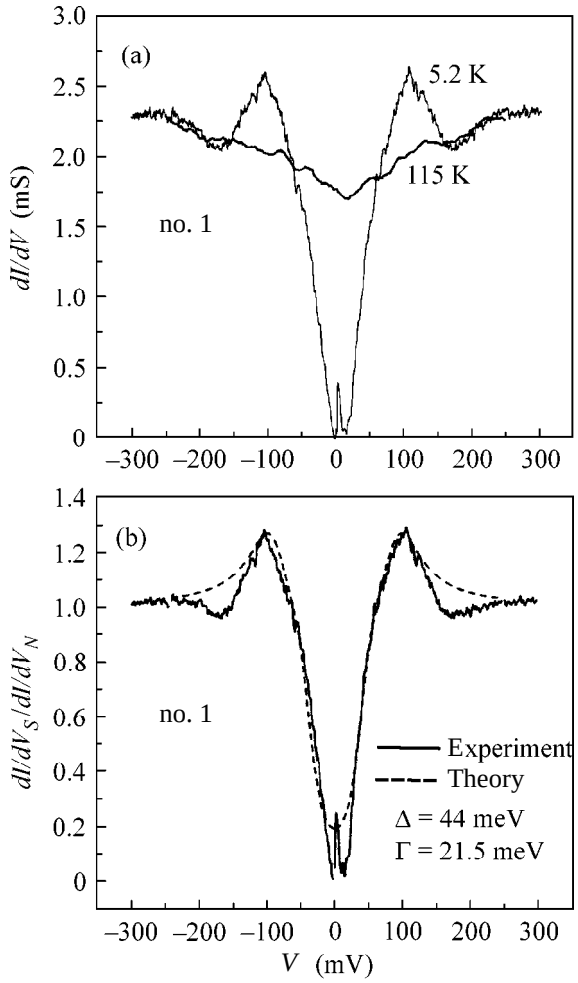

Fig. 3. (a) Smoothed tunneling conductances in superconducting $(dI/dV)_S$ (T = 5.2 K) and normal $(dI/dV)_N$ (T = 115 K) states. (b) Normalized tunneling conductance $(dI/dV)_S/(dI/dV)_N$ at T = 5.2 K (solid line) compared with the broadened BCS density of states (dashed line).

We would like to thank V.P. Martovitskii for the careful X-ray studies of the single crystals. This work was supported by the Russian Ministry of Science and Technical Policy within the Program "Actual Problems of Condensed Matter Physics" (grant no. 96001) and by the Russian Foundation for Basic Research (grant no. 99-02-17877).

REFERENCES

1. N. Miyakava, P. Guptasarma, J. F. Zasadzinski, *et al.*, Phys. Rev. Lett. **80**, 157 (1998).
2. Y. DeWilde, N. Miyakava, P. Guptasarma, *et al.*, Phys. Rev. Lett. **80**, 153 (1998).

3. R. Koltun, M. Hoffmann, P. C. Splittgerber-Hunnekes, *et al.*, Z. Phys. B: Condens. Matter **82**, 53 (1991).
4. H. J. Tao, A. Chang, Farun Lu, and E. L. Wolf, Phys. Rev. B **45**, 10622 (1992).
5. J. X. Liu, J. C. Wan, and A. M. Goldman, Phys. Rev. Lett. **67**, 2195 (1991).
6. Q. Chen, K.-W. Ng, A. E. Manzi, and H. L. Luo, Phys. Rev. B **49**, 6193 (1994).
7. S. I. Vedeneev, A. J. M. Jansen, P. Samuely, *et al.*, Phys. Rev. B **49**, 9823 (1994).
8. S. I. Vedeneev, Pis'ma Zh. Éksp. Teor. Fiz. **68**, 217 (1998) [JETP Lett. **68**, 230 (1998)].
9. J. I. Gorina, G. A. Kaljuzhnaia, V. P. Martovitsky, *et al.*, Solid State Commun. **110**, 287 (1999).
10. R. C. Dynes, V. Narayanamurti, and J. P. Carno, Phys. Rev. Lett. **41**, 1509 (1978).
11. A. Maeda, M. Hase, I. Tsukada, *et al.*, Phys. Rev. B **41**, 6418 (1990).

JETP Letters, Vol. 73, No. 3, 2001, pp. 145–148. Translated from Pis'ma v Zhurnal Éksperimental'noĭ i Teoreticheskoĭ Fiziki, Vol. 73, No. 3, 2001, pp. 163–166.

Onset of Self-Organized Critical State in a One-Dimensional Multijunction SQUID As a Result of Random Arrangement of Junctions

S. L. Ginzburg and N. E. Savitskaya

Institute of Nuclear Physics, Russian Academy of Sciences, Gatchina, Leningrad region, 188350 Russia

Received December 29, 2000

The critical state of a one-dimensional multijunction SQUID with randomly distributed junctions exposed to a slowly varying magnetic field is studied. It is shown that a small scatter of interjunction distances is sufficient for the critical state of the system to become self-organized. A simplified and basically new model is proposed for studying the self-organization in a system where this phenomenon occurs in a fully deterministic situation.

PACS numbers: 85.25.Dq; 74.50.+r

In recent years, considerable interest has been shown in the magnetic properties of granular superconductors. It was demonstrated in a number of theoretical works [1–4] that, due to the discreteness of structure of these materials, they may come, like hard type-II superconductors, into a critical state. The properties of their critical state are governed by the key parameter $V \sim j_c a^3/\Phi_0$ (a is the grain size, j_c is the critical current density in the intergrain junctions, and Φ_0 is the magnetic flux quantum).

It was shown in [5–9], both theoretically and by computer simulation, that, if V is large, then self-organized criticality—a phenomenon intensively studied in recent years [10]—can be realized in granular superconductors. This phenomenon implies that the dynamic system of an array of mutually interacting elements evolves into the critical state, which then becomes self-reproducing and persists without exact tuning of external parameters. Structurally, it represents a set of metastable states interconverting via avalanches triggered by small external perturbations. The avalanches may be both small and giant, encompassing the whole system, but both are triggered by small external actions. The avalanche sizes obey the power-law distribution. For granular superconductors, the external action is accomplished by injecting current into the system or by varying the external magnetic field. The avalanches manifest themselves in the system as voltage pulses, and the integrated avalanche voltage plays the role of avalanche size. In addition, it was shown that the simplified models of the known multijunction SQUID systems have analogues among the sandpile models, the most popular mathematical models for studying the self-organization phenomenon [10–12].

However, it was pointed out in [6–9] that the self-organization of critical state in a multijunction SQUID is possible only for certain, experimentally hard-to-realize, ways of external action or if stochastic initial conditions are introduced. For the practically most popular way of external action, namely, slow variation of an external magnetic field, the self-organization did not arise in the model. At the same time, in the experiments described in [13], the time-dependent random magnetic flux jumps with magnitudes obeying a power-law distribution were observed in the lattice of Josephson junctions precisely for this way of external action, thereby indicating that the self-organized critical state may occur in this case. This fact forced us to correct the model of multijunction SQUID. A new model presented in this paper includes the scatter of interjunction distances, as is the case in real systems.

In this work, the critical state of a one-dimensional multijunction SQUID with randomly distributed junctions exposed to a slowly varying external magnetic field is considered. It will be shown that a small scatter of the interjunction distances is sufficient for the critical state of the system to become self-organized even under conditions where the self-organization was not observed before.

We will also present a simplified and basically new model for studying the self-organization in this system. In this model, the phenomenon arises under the deterministic action on the system.

A one-dimensional multijunction SQUID represents two superconducting plates, infinite in the y direction, connected together by Josephson junctions (Fig. 1). The junctions are arranged along the x axis, and the distance between the ith and $(i + 1)$th junctions is a random variable b_i. The system is exposed to a slowly varying magnetic field H_{ext} aligned with the y axis. In the resistive model of Josephson junction with-

0021-3640/01/7303-0145$21.00

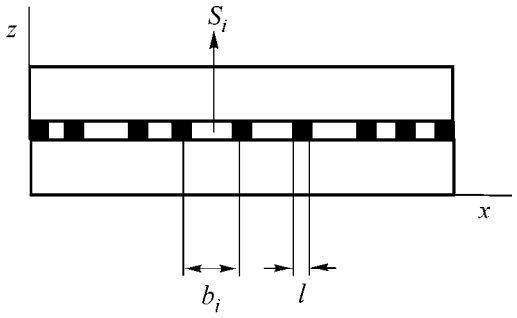

Fig. 1. (*x*, *z*) Section of a one-dimensional multijunction SQUID.

out thermal fluctuations, the current density j_i through the *i*th junction is written as

$$j_i = j_c \sin\varphi_i + \frac{\Phi_0}{2\pi\rho}\frac{\partial\varphi_i}{\partial t}, \quad (1)$$

where j_c is the critical current density, φ_i is the gauge-invariant phase difference at the *i*th junction, ρ is the surface resistivity of the junction, and Φ_0 is the magnetic flux quantum. The current density through the junction is related to the magnetic flux in the corresponding cells between the SQUID junctions as follows (the cells are numbered according to the nearest left junction):

$$4\pi j_i = \left(\frac{\Phi_i}{S_i} - \frac{\Phi_{i-1}}{S_{i-1}}\right)\frac{1}{l}, \quad (2)$$

where Φ_i is the magnetic flux in the *i*th cell, $S_i = 2\lambda_L b_i$ is the cell area, λ_L is the London penetration depth, and *l* is the junction size. Considering that the magnetic flux in the *i*th cell is related to the gauge-invariant phase difference φ_i as $\Phi_i = \frac{\Phi_0}{2\pi}(\varphi_{i+1} - \varphi_i)$, one obtains the following system of equations for the gauge-invariant phase difference:

$$V\sin\varphi_i + \tau\frac{\partial\varphi_i}{\partial t}$$

$$= [J_i\varphi_{i+1} - (J_i + J_{i-1})\varphi_i + J_{i-1}\varphi_{i-1}]; \quad i \neq 1, N,$$

$$V\sin\varphi_1 + \tau\frac{\partial\varphi_1}{\partial t} = [J_1\varphi_2 - J_1\varphi_1] - h_{\text{ext}},$$

$$V\sin\varphi_N + \tau\frac{\partial\varphi_N}{\partial t} \quad (3)$$

$$= [-J_{N-1}\varphi_N + J_{N-1}\varphi_{N-1}] + h_{\text{ext}},$$

$$V = \frac{16\pi^2 a l \lambda_L j_c}{\Phi_0}, \quad \tau = \frac{8\pi a l \lambda_L}{\rho},$$

$$J_i = \frac{a}{b_i}, \quad h_{\text{ext}} = \frac{4\pi\lambda_L a}{\Phi_0}H_{\text{ext}},$$

where *a* is the mean interjunction distance.

It was shown in [5–9] that the dynamics of the system with $V \gg 1$ can be described by introducing the discrete time $t_k = kT$, where *T* is the characteristic time of phase variation at the junctions, and replacing the system of Eqs. (3) for the gauge-invariant phase differences by the system of coupled images for the dimensionless currents flowing through the junctions $z_i = z_c\sin\varphi_i + \tau/2\pi\frac{\partial\varphi_i}{\partial t}$ ($z_c = V/2\pi$):

$$\begin{aligned}
z_i(k+1) &= z_i(k) + J_i(\theta[z_{i+1} - z_c] - \theta[-z_{i+1} - z_c]) \\
&\quad - (J_i + J_{i-1})(\theta[z_i - z_c] - \theta[-z_i - z_c]) \\
&\quad + J_{i-1}(\theta[z_{i-1} - z_c] - \theta[-z_{i-1} - z_c]); \quad i \neq 1, N. \\
z_1(k+1) &= z_1(k) + J_1(\theta[z_2 - z_c] - \theta[-z_2 - z_c]) \\
&\quad - J_1(\theta[z_1 - z_c] - \theta[-z_1 - z_c]) \\
&\quad + (h_{\text{ext}}(k) - h_{\text{ext}}(k+1))/2\pi, \\
z_N(k+1) &= z_N(k) - J_{N-1}(\theta[z_N - z_c] - \theta[-z_N - z_c]) \\
&\quad + J_{N-1}(\theta[z_{N-1} - z_c] - \theta[-z_{N-1} - z_c]) \\
&\quad + (h_{\text{ext}}(k+1) - h_{\text{ext}}(k))/2\pi.
\end{aligned} \quad (4)$$

In self-organization problems, in particular, sandpile problems, the dynamics of the system is ordinarily described by using algorithms specifying the perturbation rules and the sandpile sliding rules. The system of images (4) can also be recast as an algorithm. In this case, the z_i value plays the role of a pile slope at the *i*th site. The algorithm corresponding to Eqs. (4) is similar to the algorithm suggested in [10] for a one-dimensional sandpile.

However, since our model describes the behavior of a real physical system, it has a number of important distinctions from the model [10]. First, the perturbation is applied every time not to the accidentally chosen site but to the boundaries of the system; i.e., it is deterministic. Next, the second, negative, threshold is taken into account, as was discussed in detail in [8]. The main distinction is that the coefficients J_i in our case are random variables, whereas in [10] all J_i were identical and equal to unity.

The introduction of the random coefficients J_i is the fundamental modification of the model and leads to the appearance of the self-organized critical state under conditions for which no self-organization was obtained in the model with identical J_i [10]. The models with random coefficients have never been considered before.

We studied our model by computer simulation on a system with size $N = 2M + 1$ ($M = 64$) and with $V = 40$

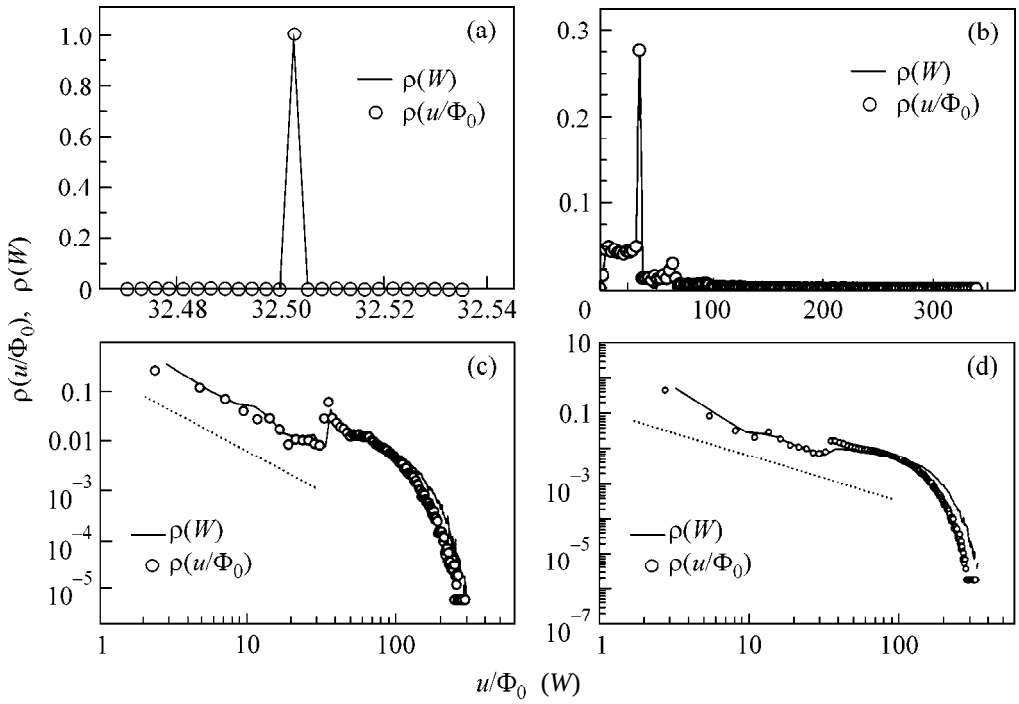

Fig. 2. Probability densities of integrated voltages for a one-dimensional multijunction SQUID; $\rho(u/\Phi_0)$ is calculated using the system of differential equations, and $\rho(W)$ is calculated using the simplified model. The interjunction distances are scattered: (a) all J_i are identical and equal to 1; (b) J_i are scattered in the range from 1 to 1.01; (c) J_i are scattered in the range from 1 to 1.2, the slope of the straight line $\alpha = -1.62$; and (d) J_i are scattered in the range from 1 to 1.4, the slope of the straight line $\alpha = -1.2$.

in the regime that is ordinarily used for studying systems with self-organization. The computations were carried out using both differential Eqs. (3) and system of images (4). As was proved in [9], both methods of system description are fully equivalent.

Before starting, we fixed the set of random J_i values, which remained constant during the simulation. Next, starting with the state for which $\varphi_i = 0$ or, what is the same, $z_i = 0$, we perturbed the system by changing the external field h_{ext} by unity, $h_{ext} \longrightarrow h_{ext} + 1$. Then, the system relaxed to the next metastable state; the h_{ext} value did not change during the relaxation. After the system had come into the next metastable state, we again perturbed it, etc.

After a time, the system reached its critical state. It represented a set of metastable states in which the currents in the right part of the system were positive and close to the critical value, while, in the left part, they were negative and close to the negative critical value. The next perturbation triggered the avalanche in the system, after which it was transferred into the next metastable state, in which the spatial structure of the system was as before, while the current magnitudes at each contact slightly changed.

For each avalanche in this critical state, we calculated the integrated avalanche voltage at the positive part of the lattice:

$$u_n = \frac{\Phi_0}{2\pi M} \sum_{i = M+2}^{N} (\varphi_i(t_{en}) - \varphi_i(t_{bn})), \qquad (5)$$

where t_{bn} and t_{en} are the instants of time corresponding to the onset and completion of the nth avalanche, respectively, and the summation is over the positive part of the lattice.

For the system of images, the analogous quantity has the form

$$W_n = \frac{1}{M} \sum_{k = k_{bn}}^{k = k_{en}} \sum_{i = M+2}^{N} (\theta[z_i(k) - z_c(k)]). \qquad (6)$$

We studied our system for different sets of J_i values. For each realization of the J_i set, we calculated the probability density $\rho(u/\Phi_0)$ or $\rho(W)$ (Fig. 2). Figure 2a shows the probability density for the case where all J_i are equal to unity; i.e., the situation is analogous to that considered in [10]. In this case, no self-organization is observed in the system and only a single metastable state occurs, to which the system returns after the next perturbation. All avalanches have the same size $u_0/\Phi_0 \approx$

32.5, and the probability density has the form of a δ function. Figure 2b illustrates the case where the J_i values are chosen at random in the interval from 1 to 1.01. One can see from Fig. 2b that the avalanches in the system have different sizes, but they are appreciably less in number than the number of avalanches of size u_0/Φ_0. As the scatter of J_i increases, the probability density becomes more and more different from the case of identical J_i, although the peak at u_0/Φ_0 is still seen (Fig. 2c). This peak disappears for the scatter in the range from 1 to 1.4, and the probability density becomes a power function with exponent close to unity (Fig. 2d). Therefore, the self-organization arises in the system without scatter of initial conditions and under fully deterministic perturbation.

The main results of this work can be formulated as follows.

It is shown that a small scatter of interjunction distances is sufficient for the one-dimensional multijunction SQUID to evolve into the self-organized critical state under the conditions corresponding to the experimental situation, namely, in a slowly varying magnetic field, where the self-organization was not observed before.

Inasmuch as the scatter of this type is inevitably present in real SQUID systems, one can conclude that their critical state is practically always self-organized.

Moreover, the suggested simplified model of the system is a basically new model for studying the self-organization, because this phenomenon arises in it in a fully deterministic situation.

We are grateful to É.V. Matizen and S.M. Ishikaev for discussion and valuable remarks. This work was supported by the Russian Foundation for Basic Research (project no. 99-02-17545), the Scientific Council of the "Superconductivity" direction of the program "Topical Directions in Physics of Condensed Media" (project no. 96021 "Profile"), the subprogram "Statistical Physics" of the state scientific and technical program "Physics of Quantum and Wave Processes" (project no. VIII-3), the state program "Neutron Studies of Matter," and (in part) the Russian Foundation for Basic Research (project no. 96-15-96775).

REFERENCES

1. T. Wolf and A. Majhofer, Phys. Rev. B **47**, 5383 (1993).
2. A. Majhofer, T. Wolf, and W. Dieterich, Phys. Rev. B **44**, 9634 (1991).
3. D.-X. Chen, J. J. Moreno, and A. Hernando, Phys. Rev. B **53**, 6579 (1996).
4. D.-X. Chen, A. Sánchez, and A. Hernando, Phys. Rev. B **50**, 13735 (1994).
5. S. L. Ginzburg, Zh. Éksp. Teor. Fiz. **106**, 607 (1994) [JETP **79**, 334 (1994)].
6. S. L. Ginzburg, M. A. Pustovoit, and N. E. Savitskaya, Phys. Rev. E **57**, 1319 (1998).
7. S. L. Ginzburg and N. E. Savitskaya, Pis'ma Zh. Éksp. Teor. Fiz. **69**, 119 (1999) [JETP Lett. **69**, 133 (1999)].
8. S. L. Ginzburg and N. E. Savitskaya, Pis'ma Zh. Éksp. Teor. Fiz. **68**, 688 (1998) [JETP Lett. **68**, 719 (1998)].
9. S. L. Ginzburg and N. E. Savitskaya, Zh. Éksp. Teor. Fiz. **117**, 227 (2000) [JETP **90**, 202 (2000)].
10. P. Bak, C. Tang, and K. Wiesenfeld, Phys. Rev. Lett. **59**, 381 (1987).
11. D. Dhar, Phys. Rev. Lett. **64**, 1613 (1990).
12. L. Kadanoff, S. R. Nagel, L. Wu, and S.-M. Zhou, Phys. Rev. A **39**, 6524 (1989).
13. S. M. Ishikaev, É. V. Matizen, V. V. Ryazanov, *et al.*, Pis'ma Zh. Éksp. Teor. Fiz. **72**, 39 (2000) [JETP Lett. **72**, 26 (2000)].

Translated by V. Sakun

JETP Letters, Vol. 73, No. 3, 2001, pp. 149–151. Translated from Pis'ma v Zhurnal Éksperimental'noĭ i Teoreticheskoĭ Fiziki, Vol. 73, No. 3, 2001, pp. 167–169.

Edge Contribution to the Electronic Energy of Cut Microcrystals

M. V. Éntin and M. M. Mahmoodian

Institute of Semiconductor Physics, Siberian Division, Russian Academy of Sciences, pr. Akademika Lavrent'eva 13, Novosibirsk, 630090 Russia

e-mail: entin@isp.nsc.ru

Received January 9, 2001

The surface part of electronic energy in small metal or semiconductor particles contains a contribution due to the presence of crystallite edges and vertices. In the approximation of quadratic electron spectrum, the edge contribution is calculated as a function of the dihedral angle of the edge and its orientation to the axes of the effective mass tensor. *© 2001 MAIK "Nauka/Interperiodica".*

PACS numbers: 72.20.Ee; 72.15.Eb

Quantum dots with a large number of electrons are an intermediate object between the quantum and classical limits. On the one hand, their size is large compared with the electron wavelength. On the other hand, the quantization of states affects the transport and thermodynamic properties of the system.

The surface contribution to the thermodynamics of a small particle with a degenerate electronic system is determined by the small ratio of the Fermi electron wavelength $1/k_F$ to the particle size L. It was shown by Nagaev *et al.* (see review [1] and references therein) that the existence of a surface leads to regular surface corrections to the chemical potential of electrons.

The existence of a surface contribution to the electron gas energy leads to diversified physical effects. In particular, it affects the surface tension in small particles and, hence, their equilibrium shapes. Establishment of an equilibrium among electron gas systems in microparticles differing in size and shape is accompanied by their spontaneous charging [1]. It is shown in [2] that the chemical potentials in microparticles are not fully equalized because of charge discreteness. This leads to the formation of a gapless dielectric state of the system of grains, that is, to a gapless Hubbard dielectric.

In addition to the surface contribution to the energy, contributions due to edges and vertices also exist in cut crystallites. The goal of this work is to find the edge contribution to the chemical potential of three-dimensional and two-dimensional cut samples.

Let us first consider a three-dimensional free electron gas bounded by a dihedral angle $0 < \varphi < \phi$, $r < R$. The electron-gas wave function ψ at the angle surface satisfies the condition[1] $\psi = 0$. We should evaluate the contribution to the Ω potential from the vicinity of an edge $r = 0$. For this purpose, let us consider the density of the Ω potential at zero temperature

$$\omega(r, \varphi) = -\sum(\mu - \varepsilon_{n,m} - k_z^2/2m_e)|\psi_{n,m}(z, r, \varphi)|^2. \quad (1)$$

Here, $\varepsilon_{n,m}$ is the electron energy level with the principal quantum number n and the magnetic quantum number m, k_z is the momentum along the edge, m_e is the electron mass, and μ is the chemical potential. The z axis is aligned with the edge.

Let the sector radius R go to infinity. In this limit, $\omega(r, \varphi)$ no longer depends on the sector size. At the same time, this quantity evidently goes to zero in the vicinity of the boundaries and the edge at distances of the order of the Fermi electron wavelength and becomes constant and equal to the bulk density of electron-gas Ω potential at long distances from the boundaries. In order to determine the edge contribution to the Ω potential, let us integrate ω over the region $r < r_0$ adjoining the edge. The result contains a volume term proportional to the volume of this region, a surface contribution proportional to the sector surface, and the r_0-independent edge contribution

$$\Omega_r = \int_0^{L_z} dz \int_0^{r_0} r dr \int_0^{\phi} d\varphi \omega$$
$$= \omega_3 L_z \phi r_0^2/2 + \omega_2 L_z r_0 + \omega_1 L_z + o(1). \quad (2)$$

[1] In principle, the problem can be solved by passing to the large volume limit from any problem with separable variables. The boundary surface should contain the dihedral angle.

With regard to the fact that the required edge contribution is absent at $\phi = \pi$, it can be found by passing to the limit

$$\omega_1 = \frac{1}{L_z}\left[\left(\Omega_r - r_0^2 \lim_{r_0\to\infty}\left[\frac{\Omega_r}{r_0^2}\right]\right)_{\phi} - \left(\Omega_r - r_0^2 \lim_{r_0\to\infty}\left[\frac{\Omega_r}{r_0^2}\right]\right)_{\phi=\pi}\right]. \quad (3)$$

The wave function obeying the boundary condition takes the form

$$\psi_{n,m}(z, r, \varphi) = C\exp(ik_z z)J_\nu(kr)\sin(\nu\varphi), \quad \nu = \pi m/\phi. \quad (4)$$

The normalization coefficient C and the energy levels can be determined if the system is bounded at a large distance $R \gg r$. Using the asymptotic form of Bessel functions at large distances

$$J_\nu(kr) \sim \sqrt{\frac{2}{\pi kr}}\cos(kr - \pi\nu/2 - \pi/4),$$

we find in the leading order in R

$$C = \sqrt{2\pi k/\phi R}, \quad \pi n = kR. \quad (5)$$

After going from the sum over n to an integral, we obtain

$$\Omega_r = -\frac{L_z}{\pi}\int_{-\infty}^{\infty} dk_z \int_0^{\infty} kdk \int_0^{r_0} rdr \times \sum_{m=1}^{\infty} J^2_{\frac{\pi m}{\phi}}(kr)\left(\mu - \frac{k^2 + k_z^2}{2m_e}\right)\theta\left(\mu - \frac{k^2 + k_z^2}{2m_e}\right). \quad (6)$$

After simple mathematics, the equation for Ω_r takes the form

$$\Omega_r = \frac{1}{m_e r_0^2}\frac{L_z}{\pi}\int_0^{k_F} dk_z u^4 \times \int_0^1 xdx\left[\ln x + \frac{1}{2}(1 - x^2)\right]\sum_{m=1}^{\infty} J^2_{\frac{\pi m}{\phi}}(ux). \quad (7)$$

Here, $u = (k_F^2 - k_z^2)^{1/2} r_0$.

The sum of Bessel functions squared can be convolved for angles $\phi = 2\pi$ and $\phi = \pi/j$, where j is an integer. Using Eq. 5.7.17.8 from [3], we obtain

$$\sum_{m=1}^{\infty} J^2_{jm}(t) = \frac{1}{j}\sum_{m=1}^{\left[\frac{j}{2}\right]} J_0\left(2t\sin\left(\frac{m\pi}{j}\right)\right) + \frac{1}{2j} - \frac{1}{2}J_0^2(t) - \frac{1}{4j}(1 + (-1)^j)J_0(2t). \quad (8)$$

In particular, at $\phi = \pi$,

$$\sum_{m=1}^{\infty} J_m^2(t) = \frac{1}{2} - \frac{1}{2}J_0^2(t), \quad (9)$$

from whence the well-known bulk and surface [1, 2] values of Ω potential can be found using the asymptotic expression at $r \longrightarrow \infty$:

$$\omega_3 = -\frac{k_F^5}{15\pi^2 m_e}, \quad \omega_2 = \frac{k_F^4}{32\pi m_e}. \quad (10)$$

The expression for ω_1 is obtained from Eqs. (3) and (7)–(9) by integration over x in the first nonvanishing quadratic order in u

$$\omega_1(\phi) = -\frac{\phi}{(2\pi)^2 m_e r_0^2} \times \int_0^{k_F} dk_z u^2\left[\sum_{m=1}^{\left[\frac{j}{2}\right]}\frac{1}{\sin^2(m\phi)} - \frac{1}{4}(1 + (-1)^j)\right]. \quad (11)$$

Summing over m, we finally obtain

$$\omega_1(\phi) = -\frac{k_F^3}{36\pi m_e}\left(\frac{\pi}{\phi} - \frac{\phi}{\pi}\right). \quad (12)$$

As is seen, at $\phi = \pi$, $\omega_1(\pi) = 0$. For the right dihedral angle, $\omega_1(\pi/2) = -k_F^3/24\pi m_e$.

The angle $\phi = 2\pi$ corresponds to a crack in the crystal. We find from Eq. (7) using Eq. 5.7.11.11 from [3] that, for this angle, $\omega_1(2\pi) = k_F^3/24\pi m_e$. This expression also satisfies Eq. (12), which was derived only for angles $\phi = \pi/j$.

A numerical calculation for arbitrary angles demonstrates an agreement with Eq. (12) to a high accuracy, which, evidently, points to its generality.

According to Eq. (12), ω_1 is negative at angles larger than π and positive at angles smaller than π. Physically, the change of sign in ω_1 is explained by the same factors as causing the positive sign of the surface contribution to the energy. The boundary region of the crystal is depleted in electrons because of the zero boundary condition. As a consequence, the region occupied by electrons is reduced, and, hence, the electron-gas energy increases at the same average density. If the boundary is bent into an angle with its area kept constant, the volume of the depleted region decreases if $\phi < \pi$ and increases if $\phi > \pi$. This leads, respectively, to a decrease or an increase in the electron-gas energy.

With the use of Eq. (12), the number of electrons in a crystallite of volume V, surface area S, and edges with

angles ϕ_n and lengths L_n is expressed through the chemical potential

$$N = -\frac{\partial\Omega}{\partial\mu} = \frac{(2m_e\mu)^{\frac{3}{2}}V}{3\pi^2} - \frac{m_e\mu S}{4\pi} + \frac{(2m_e\mu)^{\frac{1}{2}}}{12\pi}\sum_n L_n\left(\frac{\pi}{\phi_n} - \frac{\phi_n}{\pi}\right). \quad (13)$$

The expression for the edge contribution to the energy allows a simple generalization to the case of an anisotropic quadratic energy spectrum $\varepsilon(k) = \sum k_i^2/2m_i$. Let us consider a particular case when the edge coincides with the axis (3) of the effective mass ellipsoid. Let α and β be the angles of crystallite edges with the *xz* plane. With the use of an affine transformation $x_i' = x_i(m_i/m_e)^{1/2}$, where $m_e = (m_1m_2m_3)^{1/3}$, the Schrödinger equation is transformed to an isotropic form, for which all above consideration is valid. In this case, the transformed dihedral angle entering into the above equations is defined by the relationship

$$\tan\phi = \sqrt{\frac{m_2}{m_1}}\frac{\tan\alpha - \tan\beta}{1 + \frac{m_2}{m_1}\tan\alpha\tan\beta}, \quad (14)$$

and the edge length L_n is replaced by $L_n\sqrt{m_3/m_e}$.

Equation (12) was derived for an edge of a three-dimensional crystal. Analogous problems also arise in considering bounded two-dimensional systems in which the motion along the *z* axis is quantized. A transition to two-dimensional formulas can be accomplished by excluding the integration over k_z and the multiplier $L_z/2\pi$ in the intermediate formulas. As a result, the energy of an angle of a two-dimensional area takes the form

$$\omega_1(\phi) = -\frac{k_F^2}{24m_e}\left(\frac{\pi}{\phi} - \frac{\phi}{\pi}\right). \quad (15)$$

Computer calculations of energy states in many-electron quantum dots are a rather complicated problem, because the number of energy states included in the Hamiltonian matrix grows exponentially with increasing number of electrons. At the same time, simple estimates can be obtained, without tedious computations, by using the approach considered here, which is based on a power expansion of thermodynamic quantities in terms of the system size. In particular, the occupation numbers of so-called self-organized quantum dots of one semiconductor on the surface of another, which are commonly shaped as cut pyramids (see, for example, [4]), can be readily estimated with the use of this approach.

This work was supported by the Russian Foundation for Basic Research (project no. 00-02-17658) and by the Russian Federation State Program "Physics of Solid-State Nanostructures."

REFERENCES

1. É. L. Nagaev, Usp. Fiz. Nauk **162** (9), 49 (1992) [Sov. Phys. Usp. **35**, 747 (1992)].
2. É. M. Baskin and M. V. Éntin, Pis'ma Zh. Éksp. Teor. Fiz. **70**, 511 (1999) [JETP Lett. **70**, 520 (1999)].
3. A. P. Prudnikov, Yu. A. Brychkov, and O. I. Marichev, *Integrals and Series* (Nauka, Moscow, 1981, 1983, 1986; Gordon and Breach, New York, 1986, 1986, 1989), Vols. 1–3.
4. Pu Liu, J. M. Gibson, D. G. Cahill, *et al.*, Phys. Rev. Lett. **84**, 1958 (2000).

Translated by A. Bagatur'yants

JETP Letters, Vol. 73, No. 3, 2001, pp. 152–155. Translated from Pis'ma v Zhurnal Éksperimental'noĭ i Teoreticheskoĭ Fiziki, Vol. 73, No. 3, 2001, pp. 170–174.

Synchronous Electron–Nuclear Vibrations in a π-Conjugated Nanopoly(acetylene) Chain

D. Yu. Paraschuk* and V. M. Kobryanskiĭ**

** Faculty of Physics, Moscow State University, Vorob'evy gory, Moscow, 119899 Russia*

e-mail: paras@polys.phys.msu.su

*** Semenov Institute of Chemical Physics, Russian Academy of Sciences, ul. Kosygina 4, Moscow, 117997 Russia*

Received January 10, 2001

An unusual behavior was observed for the spontaneous Raman spectra in the range of the passband of *trans*-poly(acetylene) nanoparticles. The following phenomena are observed for the stretching carbon–carbon vibrations: large scattering cross section; high anti-Stokes-to-Stokes ratio; no correlation between the absorption spectra of *trans*-nanopoly(acetylene) and the Raman excitation spectrum. A qualitative model is proposed for synchronous weakly damping electron–nuclear vibrations in the ordered poly(acetylene) chain. © *2001 MAIK "Nauka/Interperiodica".*

PACS numbers: 63.22.+m; 71.45.-d; 78.30.Jw; 78.66.Qn

Over the last few decades, the properties of polymer chains containing a system of conjugated π-electron bonds have attracted attention of both chemists and physicists. The dynamics of relatively weakly bonded π electrons (as compared to σ electrons) in the conjugated chain is quasi-one-dimensional, leading to highly anisotropic properties, both optical and conducting, of π electrons. Poly(acetylene) $(CH)_x$ is the chemically most simple π-conjugated polymer (Fig. 1, inset), whose backbone is formed by the localized σ bonds and in which the atomic orbitals of nonhybridized *p* electrons of the nearest carbon sites overlap to form a delocalized π-electron system. The π-electron density between the adjacent carbon sites contributes to the energy of localized σ electrons, thereby sizably affecting the carbon–carbon bond strength; i.e., the *trans*-$(CH)_x$ chain is characterized by strong electron–phonon interaction. In this work, we report the unusual, for the conventional theory of spontaneous Raman scattering (SRS), behavior of the spectrum of C–C and C=C stretching vibrations in nanopoly(acetylene) [nano-$(CH)_x$] samples. We also suggest a qualitative model of synchronous electron–nuclear vibrations in the *trans*-$(CH)_x$ chain and use it in interpreting the experimental result. The main features observed in the SRS spectra are as follows: the SRS cross sections and the intensity ratios between the anti-Stokes and Stokes components are unexpectedly large if nano-$(CH)_x$ samples are excited in the range of the passband; moreover, no correlation is observed between the absorption spectrum and the SRS excitation spectrum.

The ground-state geometry of an ideal infinite *trans*-$(CH)_x$ chain represents a sequence of almost equidistant carbon sites (the difference between the C=C and C–C bond lengths is small) and a coplanar zigzag formed by σ bonds (Fig. 1, inset). Such a model of an ideal infinite chain is based on the most adequate *ab initio* calculations of the short poly(acetylene) chains (polyenes). A value of ~0.05 Å obtained by these calculations for the difference between the C–C and C=C bonds (alternation parameter) at the midpoint of the chain is comparable with the quantum nuclear fluctuations in an isolated C=C bond. The distinctions between the geometry and energy spectrum of the real and ideal π-conjugated chains are mainly caused by two factors: the chain-end and environmental effects. The chain ends are almost isolated C=C bonds, which obtrude the bond-length alternation upon the nearest bonds. At the same time, numerical computations suggest that the chain-end effect rapidly dies down at distances of a few carbon–carbon bonds. Furthermore, the real chains usually reside in a solvent or are surrounded by the same chains. For the chains in a solution, the environmental effect manifests itself as a fluctuating local field. The solvent molecules affect each of the cells (e.g., the C=C bond) differently, making the C=C bond strengths in the chain different. This, in turn, suppresses the translational order in the chain and drastically reduces the π-conjugation efficiency. Analogous effects also occur in the real $(CH)_x$ samples consisting of a set of chains with a broad distribution of conjugation lengths. It turned out that best ordered $(CH)_x$ chains are present in the nano-$(CH)_x$ samples where the conjugated bonds are assembled together as nanoparticles dispersed in a matrix of saturated polymer [1]. The conjugated chains in nano-$(CH)_x$ have a modest length, no longer than 30 nm, but are characterized by a narrow length distribution and low concentration of conjugation defects [2, 3]. The unusual features observed by us in the SRS

spectra of *trans*-nano-$(CH)_x$ are due precisely to the latter fact.

Let us briefly summarize the known data on the SRS spectroscopy of conjugated chains. In 1950s, it was found from the SRS experiments on polyenes containing several carbon–carbon bonds that the addition of each new C=C cell dramatically increased the SRS intensity [4] in the range of stretching C–C and C=C vibrations, usually denoted, respectively, as ν_1 and ν_3. Another important effect was investigated in detail in the last few decades. It consists in the lowering of the ν_1 and ν_3 frequencies with an increase in the chain length [5]. It was realized in [6, 7] that these facts are due to the π- conjugation effect, because it is associated with the delocalization of π electrons and, hence, "washes away" electron density from the C=C-bond region, making the C=C bonds softer.

Let us now describe the model of synchronous electron–nuclear vibrations in the *trans*-$(CH)_x$ chain. The increase in the Raman activity of the ν_1 and ν_3 modes of the *trans*-$(CH)_x$ chain can naturally be explained by the fact that the chain of coupled oscillators has a collective center-zone optical mode corresponding to the antiphase vibrations of the adjacent C=C and C–C bonds and, accordingly, in-phase vibrations of all C=C and all C–C bonds in the chain. Among the chain modes, this type of vibrations will provide the greatest modulation of the π-electron polarizability and, hence, the highest Raman activity. Indeed, within the framework of the one-electron model, the *trans*-$(CH)_x$ chain (Fig. 1, inset) with identical carbon–carbon bond lengths will be metallic, while the alternating chain will be a semiconductor because the unit cell in the latter case will include two carbon sites and two π electrons. If the C=C and C–C vibrations are in antiphase synchronously in all chain cells, then the optical band gap and the polarizability are strongly modulated. With real $(CH)_x$ samples, such in-phase vibrations can occur in the central part of a long conjugated chain. It is clear that the SRS intensity due to the synchronous vibrations will sharply increase with increasing chain length, because not the intensities but vibrational amplitudes add up in this case. Evidently, the closer the frequencies of the adjacent C=C cells and the larger the number of such cells in the central part of the chain, the more probable the effect of synchronization of the vibrations of coupled oscillators. This effect is analogous to the effect of passive mode-locking in lasers. The structural and thermal disorder will misphase the chain synchronous vibrations. A structural defect, e.g., in the form of a sp^3-hybridized carbon site in the chain, will "disrupt" the π conjugation because it sharply decreases the overlap of π-electron wave functions at the carbon sites surrounding the defect. This will strongly suppress the π-electron delocalization. Similarly, the thermal disorder is mainly associated with the out-of-plane chain modes and also sharply reduces the conjugation efficiency.

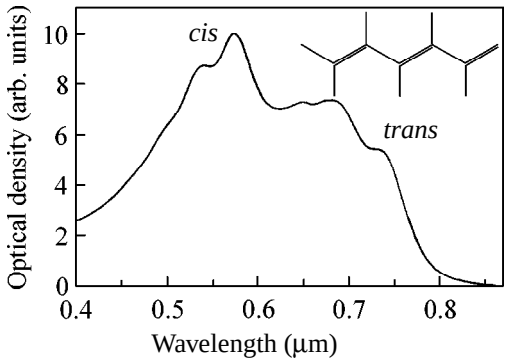

Fig. 1. Absorption spectrum of the nano-$(CH)_x$ film at room temperature; *trans* and *cis* indicate zero-phonon lines of the *trans* and *cis* isomers, respectively. The geometry of a chain fragment of the *trans* isomer is shown in the inset.

The SRS spectra were recorded at room temperature with different spectrometers at several excitation wavelengths in the range 1064–488 nm [8, 9] using "reflection" scattering geometry. The $(CH)_x$ content in (2–50)-μm-thick poly(vinyl butyral) films was ~1%. Liquid samples were taken as highly diluted butanol–poly(vinyl butyral)–$(CH)_x$ nanoparticle solutions. The concentrations of *cis* and *trans* isomers in nano-$(CH)_x$ were estimated at 50%/50%. In what follows, only three experimental observations are discussed for the ν_1 and ν_3 lines: (i) large SRS cross section for the *trans* isomer in the range of the passband; (ii) SRS excitation spectrum; and (iii) high anti-Stokes-to-Stokes ratio for the *trans* isomer excited in the range of the passband.

(i) It was found that the SRS cross section was unexpectedly large for *trans*-nano-$(CH)_x$ excited in the range of the passband. The SRS spectrum of a liquid sample (Fig. 2) was used to estimate the SRS cross section for *trans*-nano-$(CH)_x$ relative to the most intense band at ~2900 cm^{-1} due to the associated C–H bonds of the solvent. For the *trans*-nano-$(CH)_x$ volume concentration of $\sim 2 \times 10^{-4}$ in the solvent and with regard to the correction factor "ω^4," one finds from Fig. 2 that the integrated SRS cross section for *trans*-nano-$(CH)_x$ is four orders of magnitude larger than the SRS cross section for quite strong solvent lines [10]. The SRS cross section for *trans*-nano-$(CH)_x$ in the range of the passband is large to an extent that rather resembles resonance SRS. However, nano-$(CH)_x$ is transparent at a wavelength of 1064 nm; photothermal measurements show[1] that the absorption of nano-$(CH)_x$ is at least four orders of magnitude weaker than the absorption in the range of the fundamental dipole-transition band of *trans*-nano-$(CH)_x$ (Fig. 1).

(ii) Figure 3 shows the SRS spectra of the *trans* and *cis* isomers for four excitation wavelengths 1064, 647,

[1] Unpublished data of N.V. Chigarev and one of the authors (D.Yu.P.).

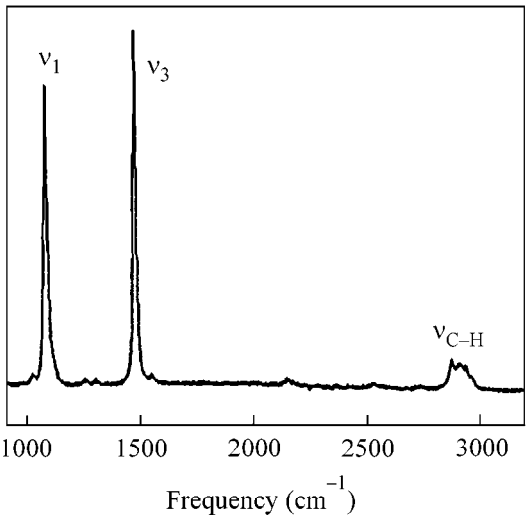

Fig. 2. SRS spectrum of a solution of nano-$(CH)_x$ for the excitation wavelength of 1064 nm.

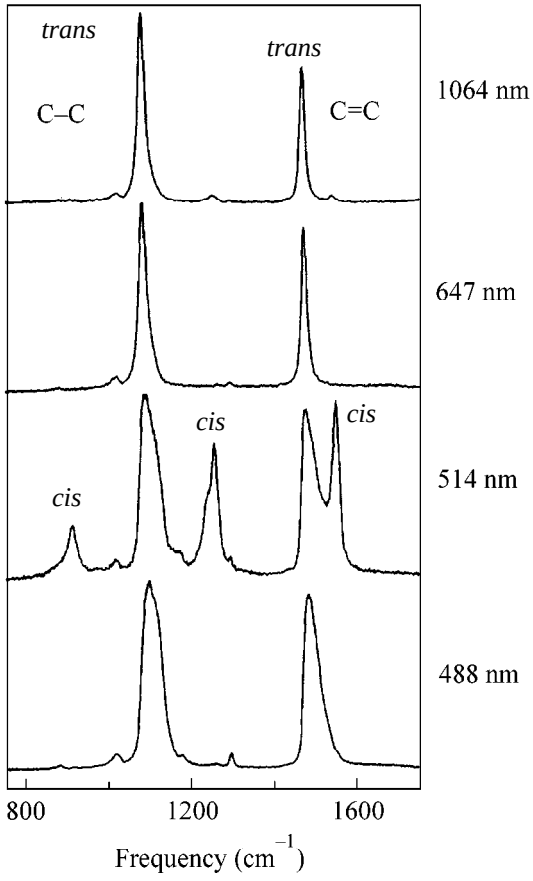

Fig. 3. SRS spectra of the nano-$(CH)_x$ films for four excitation wavelengths.

514, and 488 nm. A comparison of these spectra with the absorption spectra of the *trans* and *cis* isomers (Fig. 1) shows that the intensities of the *cis* SRS lines are the greatest, relative to the *trans* lines, for the excitation wavelength closest to the absorption maximum of the *cis* isomer (514 nm). For the other excitation wavelengths, the *cis* lines are at least an order of magnitude weaker than the lines of the *trans* isomer. An unusual fact is that the line intensities of the *trans* isomer correlate with its absorption spectrum for none of the excitation wavelengths; in other words, the SRS excitation spectrum of *trans*-nano-$(CH)_x$ is "insensitive" to the fundamental dipolar absorption band. Note that the integrated SRS cross section for the Stokes components always increased linearly with a rise in the excitation intensity [9].

(iii) Figure 4 shows the Stokes and anti-Stokes SRS components of nano-$(CH)_x$ for the excitation wavelength of 1064 nm. Within the framework of the nonresonance SRS model, the observed high intensity ratio between the anti-Stokes and Stokes scattering components corresponds to the effective vibrational temperature of about 700 K, which is considerably higher than the destruction temperature of $(CH)_x$.

We relate high Raman activity of the ν_1 and ν_3 modes to the synchronous vibrations of the *trans*-nano-$(CH)_x$ chain. In this case, the SRS cross section increases to a level characteristic of the resonance RS where the exciting photon falls within the absorption band. The high ratio between the anti-Stokes and Stokes components can reasonably be attributed to the nonthermal population of the ν_1 and ν_3 modes. The population will be effective if the lifetime of the synchronous ν_1 and ν_3 modes is such that they do not decay during the time interval between the scattering events. Note that this anti-Stokes scattering mechanism corresponds to the four-photon process underlying CARS spectroscopy. In [11], detailed measurements of the SRS excitation spectrum were performed for deeply cooled *trans*-β-carotene, a finite analogue of *trans*-$(CH)_x$ with nine C=C cells. For the absorption band and below it, the SRS excitation spectrum measured from the ν_3 (C=C) mode of the ordered samples represented a Franck–Condon sequence, with the SRS cross section being the same both in the absorption peak and several linewidths below it. For the less ordered samples, e.g., β-carotene in a solution, the SRS cross section sharply decreased near the absorption band [11]. A high SRS cross section in the ordered β-carotene microcrystals can naturally be related to the synchronous vibrations of the C=C bonds in the cells of the β-carotene chain. Thus, one can conclude that the effect of coherent electron–nuclear motion is observable for ordered polyene chains containing even ~10 C=C bonds.

Therefore, due to the π-electron subsystem, the vibrations of the carbon–carbon bonds in the ordered *trans*-$(CH)_x$ chain are synchronized over its extended section, leading to the enhanced Raman activity of the ν_1 and ν_3 modes. The characteristic length L of this section can be estimated as a length for which the electron

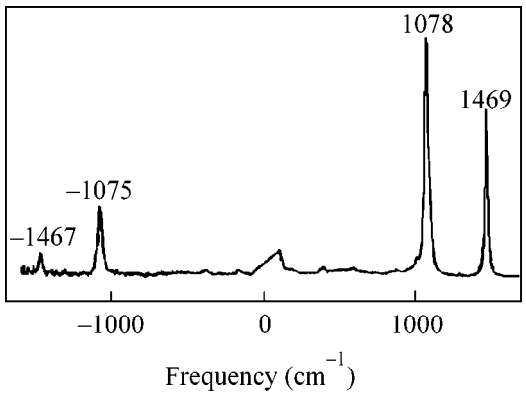

Fig. 4. SRS spectrum of the nano-$(CH)_x$ film for the excitation wavelength of 1064 nm. Excitation intensity is <20 kW/cm^2.

passage time with Fermi velocity $V_F \sim 1.5 \times 10^8$ cm/s [5] is comparable with the period of ν_3 vibrations; i.e., $L \sim V_F/\nu_3 \simeq 300$ Å. Consequently, L corresponds to a chain containing ~100 C=C bonds, i.e., is on the order of the characteristic size of the nano-$(CH)_x$ nanoparticle. Note that the analogous effect of enhanced activity of the vibrational modes correlated with the oscillations of π-electron density is observed in the IR spectra of aromatic hydrocarbons and is also assigned to the collective electron–nuclear motions extended over the whole conjugated molecule [12]. Moreover, the lifetime of synchronous vibrations in the π-conjugated systems may be rather long. For instance, weakly damping C–C, C=C, and C≡C vibrations were observed in the π-conjugated chain of poly(diacetylene) excited by a 5-fs optical pulse [13]. It should be emphasized that the photoinduced states in the π-conjugated chains, in particular, *trans*-nano-$(CH)_x$, are characterized by more than one time constant up to the millisecond time scale [2]. An important point is that on cooling *trans*-nano-$(CH)_x$, i.e., reducing the concentration of thermal defects in the chain, the conjugated chain tends to change its structure, as is evident from the splitting of the SRS ν_3 line [3]. Therefore, it is quite probable that the well-ordered π-conjugated chain can undergo phase transition to the state with undamped vibrations, i.e., correlated electron–nuclear motion without scattering.

This work was supported in part by the Russian Foundation for Basic Research, project no. 99-02-17785.

REFERENCES

1. V. M. Kobryanskii and E. A. Tereshko, Synth. Met. **39**, 367 (1991).
2. D. Yu. Paraschuk, T. A. Kulakov, and V. M. Kobryanskii, Phys. Rev. B **50**, 907 (1994).
3. D. Yu. Paraschuk, S. A. Arnautov, A. N. Shchegolikhin, and V. M. Kobryanskii, Pis'ma Zh. Éksp. Teor. Fiz. **64**, 613 (1996) [JETP Lett. **64**, 658 (1996)].
4. M. M. Sushchinsky, *Raman Scattering Spectra of Molecules and Crystals* (Nauka, Moscow, 1969; Israel Program for Scientific Translations, Jerusalem, 1973).
5. A. J. Heeger, S. Kivelson, J. R. Schrieffer, and W.-P. Su, Rev. Mod. Phys. **60**, 781 (1988).
6. M. Gussoni, C. Castiglioni, and G. Zerbi, in *Spectroscopy of Advanced Materials*, Ed. by R. J. H. Clark and R. E. Hester (Wiley, New York, 1991).
7. Z. V. Vardeny, E. Ehrenfreund, O. Brafman, and B. Horovitz, Phys. Rev. Lett. **51**, 2326 (1983); Phys. Rev. B **36**, 1535 (1987).
8. V. M. Kobryanskiĭ, Dokl. Akad. Nauk **362**, 213 (1998).
9. V. M. Kobryanskii, D. Yu. Paraschuk, A. N. Shchegolikhin, *et al.*, Proc. SPIE **4098** (2000) (in press).
10. B. Schrader, *Raman/Infrared Atlas of Organic Compounds* (VCH, Basel, 1989), A3-06.
11. H. Hashimoto, Y. Koyama, and Y. Mori, Jpn. J. Appl. Phys., Part 2 **36**, L916 (1997).
12. H. Torii, Vib. Spectrosc. **24**, 3 (2000).
13. T. Kobayashi, A. Shirakawa, H. Matsuzawa, and H. Nakanishi, Chem. Phys. Lett. **321**, 385 (2000).

Translated by V. Sakun